

# JGR Planets

## RESEARCH ARTICLE

10.1029/2019JE006320

### Special Section:

Investigations of Vera Rubin Ridge, Gale Crater

### Key Points:

- A decrease in Li and Chemical Index of Alteration, reflecting clay mineral content, is observed across Vera Rubin ridge (VRR)
- A Mn-rich interval is observed stratigraphically above the decrease in clay mineral content on VRR
- VRR likely resulted from increased induration from late-stage fluid interactions long after the lake environment in Gale crater ceased

### Supporting Information:

- Supporting Information S1
- Data Set S1

### Correspondence to:

J. Frydenvang,  
jfrydenvang@snm.ku.dk

### Citation:
























Frydenvang, J., Mangold, N., Wiens, R. C., Fraeman, A. A., Edgar, L. A., Fedo, C. M., et al. (2020). The chemostratigraphy of the Murray Formation and role of diagenesis at Vera Rubin Ridge in Gale Crater, Mars, as observed by the ChemCam instrument. *Journal of Geophysical Research: Planets*, 125, e2019JE006320. <https://doi.org/10.1029/2019JE006320>

Received 7 DEC 2019

Accepted 22 JUN 2020

Accepted article online 27 JUN 2020

## The Chemostratigraphy of the Murray Formation and Role of Diagenesis at Vera Rubin Ridge in Gale Crater, Mars, as Observed by the ChemCam Instrument

J. Frydenvang<sup>1</sup> , N. Mangold<sup>2</sup> , R. C. Wiens<sup>3</sup> , A. A. Fraeman<sup>4</sup> , L. A. Edgar<sup>5</sup> , C. M. Fedo<sup>6</sup> , J. L'Haridon<sup>2</sup> , C. C. Bedford<sup>7,8</sup> , S. Gupta<sup>9</sup> , J. P. Grotzinger<sup>10</sup> , J. C. Bridges<sup>11</sup> , B. C. Clark<sup>12</sup> , E. B. Rampe<sup>8</sup> , O. Gasnault<sup>13</sup> , S. Maurice<sup>13</sup> , P. J. Gasda<sup>3</sup> , N. L. Lanza<sup>3</sup> , A. M. Olilla<sup>3</sup> , P.-Y. Meslin<sup>13</sup> , V. Payré<sup>14</sup> , F. Calef<sup>4</sup> , M. Salvatore<sup>15</sup> , and C. H. House<sup>16</sup> 

<sup>1</sup>Globe Institute, University of Copenhagen, Copenhagen, Denmark, <sup>2</sup>LPG, Université de Nantes, Nantes, France,

<sup>3</sup>Los Alamos National Laboratory, Los Alamos, NM, USA, <sup>4</sup>Jet Propulsion Laboratory, California Institute of Technology, Pasadena, CA, USA, <sup>5</sup>U. S. Geological Survey, Flagstaff, AZ, USA, <sup>6</sup>Department of Earth and Planetary Sciences, University of Tennessee, Knoxville, TN, USA, <sup>7</sup>Lunar and Planetary Institute, Universities Space Research Association, Houston, TX, USA, <sup>8</sup>NASA Johnson Space Center, Houston, TX, USA, <sup>9</sup>Department of Earth Science & Engineering, Imperial College London, London, UK, <sup>10</sup>Division of Geological and Planetary Sciences, California Institute of Technology, Pasadena, CA, USA, <sup>11</sup>School of Physics and Astronomy, University of Leicester, Leicester, UK, <sup>12</sup>Space Science Institute, Littleton, CO, USA, <sup>13</sup>Institut de Recherche en Astrophysique et Planétologie, Université de Toulouse, CNRS, CNES, UPS, Toulouse, France, <sup>14</sup>Department of Earth, Environmental, and Planetary Science, Rice University, Houston, TX, USA, <sup>15</sup>Department of Astronomy and Planetary Science, Northern Arizona University, Flagstaff, AZ, USA, <sup>16</sup>Department of Geosciences and Earth and Environmental Systems Institute, Pennsylvania State University, State College, PA, USA

**Abstract** Geochemical results are presented from Curiosity's exploration of Vera Rubin ridge (VRR), in addition to the full chemostratigraphy of the predominantly lacustrine mudstone Murray formation up to and including VRR. VRR is a prominent ridge flanking Aeolis Mons (informally Mt. Sharp), the central mound in Gale crater, Mars, and was a key area of interest for the Mars Science Laboratory mission. ChemCam data show that VRR is overall geochemically similar to lower-lying members of the Murray formation, even though the top of VRR shows a strong hematite spectral signature as observed from orbit. Although overall geochemically similar, VRR is characterized by a prominent decrease in Li abundance and Chemical Index of Alteration across the ridge. This decrease follows the morphology of the ridge rather than elevation and is inferred to reflect a nondepositionally controlled decrease in clay mineral abundance in VRR rocks. Additionally, a notable enrichment in Mn above baseline levels is observed on VRR. While not supporting a single model, the results suggest that VRR rocks were likely affected by multiple episodes of postdepositional groundwater interactions that made them more erosionally resistant than surrounding Murray rocks, thus resulting in the modern-day ridge after subsequent erosion.

**Plain Language Summary** Results from the ChemCam instrument on Vera Rubin ridge (VRR) in Gale crater, Mars, are presented and compared with observations from similar rocks leading up to the ridge. VRR is a prominent ridge, flanking the central mound, Aeolis Mons, in Gale crater, Mars. The ridge attracted early attention because it displays strong iron-oxide spectral signatures. Surprisingly, ChemCam data show that VRR rocks do not show an overall increase in iron abundance relative to the comparable bedrock analyzed for almost 300 m in elevation leading up to the ridge. While similar overall, some notable variations were observed on VRR relative to lower-lying rocks. In particular, geochemical variations suggest a strong decrease in clay content on the ridge, above which, a notable enrichment in Mn is observed. No single geological process confidently explains all observations on the ridge. Rather, we think that VRR rocks underwent a series of interactions with groundwater that caused the rocks of VRR to become more resistant to erosion than their surroundings, thus emerging as a ridge as the rocks around them eroded. This likely implies that groundwater persisted in Gale crater even long after the disappearance of the ancient lake.

## 1. Introduction

The primary objective of the Mars Science Laboratory (MSL) mission is to investigate whether Mars ever had a habitable environment. To address this, the approximately 150-km diameter Gale crater (4.6°S, 137.4°E)

was selected as the landing site for MSL's Curiosity rover. Gale crater is a deep basin that drops to more than 5 km below the Martian datum, and fluvial channels lead into the crater that locally terminate as alluvial fans (Grotzinger & Milliken, 2012; Milliken et al., 2010; Palucis et al., 2014). A 5-km-tall mound, formally named Aeolis Mons (informally, Mount Sharp), is at the center of the crater. Orbital spectral observations indicate a sequence of stratified secondary mineral signatures on the lower slopes of Mount Sharp that include hematite, clays, and sulfates. Collectively, this sequence of stratified rocks is referred to as the Mount Sharp group. The upper part of Mount Sharp only shows spectral evidence for anhydrous material (Fraeman et al., 2016; Milliken et al., 2010; Thomson et al., 2011). From orbital observations, it was hypothesized that the lower part of Mount Sharp provides a geological record of an ancient aqueous environment in Gale crater that gradually ceased as Mars became colder and drier (Milliken et al., 2010). In situ observations of Murray formation rocks, the lowermost exposed stratigraphic unit of the Mount Sharp group, confirmed that these reflect an ancient fluvio-lacustrine habitable environment (Fedo et al., 2019; Grotzinger et al., 2015; Stack et al., 2019). How long this habitable environment persisted on Mars remains a key outstanding question for the ongoing MSL mission.

On Mars solar day (sol) 1809 of the MSL mission (August 2017), the Curiosity rover arrived at the base of Vera Rubin ridge (VRR), a kilometer-long and approximately 200-m-wide ridge on the northwestern slopes of Mount Sharp (Figure 1a). The subsequent main phase of the VRR campaign consisted of the approximately 500 sols between arriving at the ridge until the Curiosity rover drove off the ridge to the south on sol 2302, entering the Glen Torridon area that displays prominent clay mineral spectral signatures from orbit (Figure 1a; Anderson & Bell, 2010; Fraeman et al., 2013, 2016). VRR attracted substantial early attention because it is associated with a strong hematite spectral signature from orbit that traces the top of the ridge (Fraeman et al., 2013, 2016; Milliken et al., 2010). Analysis of the orbital data suggested that the ridge could preserve a redox interface and, therefore, a potential past habitable environment (Fraeman et al., 2013). For this reason, a considerable time investment was made to characterize the geological origin of VRR and understand its implications for the past habitable environment on Mars. Our investigations of VRR include two independent (N-S) traverses of the full stratigraphy of VRR (Figures 1c and 1d), which enabled spatial mapping of both the stratigraphic and geochemical variations across the ridge.

This manuscript presents the geochemical variations observed on VRR as observed with the ChemCam ("Chemistry and Camera") instrument (Maurice et al., 2012; Wiens et al., 2012). To provide the necessary context for evaluating the geochemical variations on VRR, the complete data set of comparable ChemCam bedrock observations from the traverse leading up to VRR is also presented. Lastly, possible formation scenarios for VRR are discussed.

## 2. Geological Context

The Murray formation was first encountered by Curiosity around sol 750 at the Pahrump Hills location (Figure 1b). In situ observations of Murray formation bedrock along the approximately 11-km traverse from Pahrump Hills to VRR reveal that it primarily consists of planar laminated mudstone (Fedo et al., 2019; Grotzinger et al., 2015; Stack et al., 2019). The dip of the Murray formation is observed to be close to horizontal, so elevation is considered a good proxy for stratigraphic thickness (Grotzinger et al., 2015; Stein et al., 2020). Hence, Curiosity is interpreted to have climbed through more than ~250 m of Murray formation stratigraphy leading up to the base of VRR.

Our high-level understanding of the geological evolution of Gale crater is detailed in Grotzinger et al. (2015) and Stack et al. (2019) and involves multiple episodes of deposition, burial, and exhumation. Rocks comprising the Murray formation were deposited in lacustrine and lacustrine-margin environments, which were buried, exhumed, and eroded into the topography that now exposes the members of the Murray formation (Grotzinger et al., 2015). The unconformably overlying eolian Stimson formation sandstone of the Siccar Point group (Banham et al., 2018) provides evidence for at least one additional episode of burial and erosion because it drapes the Murray formation at the Emerson and Naukluft plateaus (Figures 1b and 2). ChemCam observations from the much younger Stimson formation (see, e.g., Bedford et al., 2020) are not included in the data presented here and thus appear as gaps in the overview of ChemCam Murray formation observations (Figure 1b).



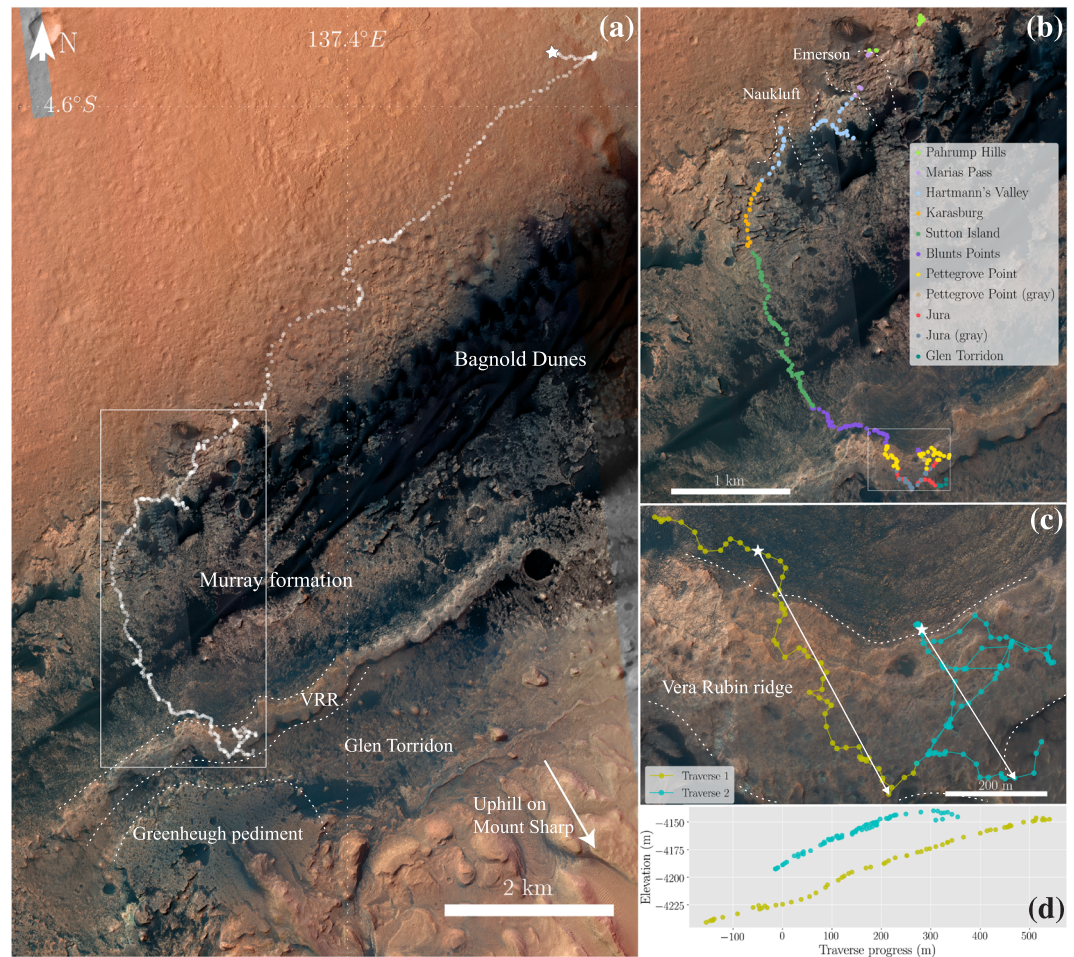


**Figure 1.** (a) The traverse of the Curiosity rover from the landing site (noted with star) to the end-of-drive location on sol 2,315 of the mission, shortly after the rover drove off Vera Rubin ridge and into the Glen Torridon area. The Vera Rubin ridge (VRR), the Greenheugh pediment, and the Glen Torridon area have been annotated. The box indicates the area shown in (b) and represents where the Murray formation has been analyzed. The top part of the map depicts the trough of Gale crater, with the elevation increasing steadily toward the bottom right of the image. The darkest patches are the eolian sands of the Bagnold dunes. (b) ChemCam observation points assigned to Murray formation members from the first observation at the Pahrump Hills location and including observations from the first 12 sols after the Curiosity rover entered the Glen Torridon area. The gaps in the observation points in Hartmann's Valley and Marias Pass are where the rover drove onto the eolian Stimson formation Emerson and Naukluft plateaus (outlined). The box indicates the area shown in (c) where Curiosity investigated VRR. (c) The rover drive locations at and on VRR are shown together with representations of the two traverse paths across VRR (white arrows). The first traverse extends to the highest elevation reached on the first ascent. The second traverse includes the descent to down (north) below the ridge and the subsequent ascent until leaving the ridge and entering the Glen Torridon area to the south. (d) Elevation of each rover location plotted against traverse progress along each traverse. For each traverse, the drive locations are projected onto the indicated path in Figure 1c with the relevant star indicating the origin. The resulting transects of VRR show that the observed base of the ridge starts at different elevations in different locations. Additionally, while VRR is a shoulder on the side of Mt. Sharp, the area south of VRR is considerably higher in elevation than the area north of the ridge. (a)–(c) are based on a mosaic of HiRISE images of Gale crater, Mars; see Calef and Parker (2016) for details.

The Murray formation, up to VRR, is subdivided into five lithostratigraphic members: The Pahrump Hills, Hartmann's Valley, Karasburg, Sutton Island, and Blunts Point members (see Fedo et al., 2019; Siebach et al., 2019, for details, Figures 1 and 2). ChemCam data of the Murray formation bedrock will be classified as belonging to the relevant lithostratigraphic member, but some additional subdivisions are informally added to visualize and track features observed along the traverse up Mount Sharp. One such subdivision is the upper part of the Pahrump Hills member, which displays a distinct geochemistry and mineralogy compared to both the lower part of the Pahrump Hills member and the Murray formation in general (Rampe

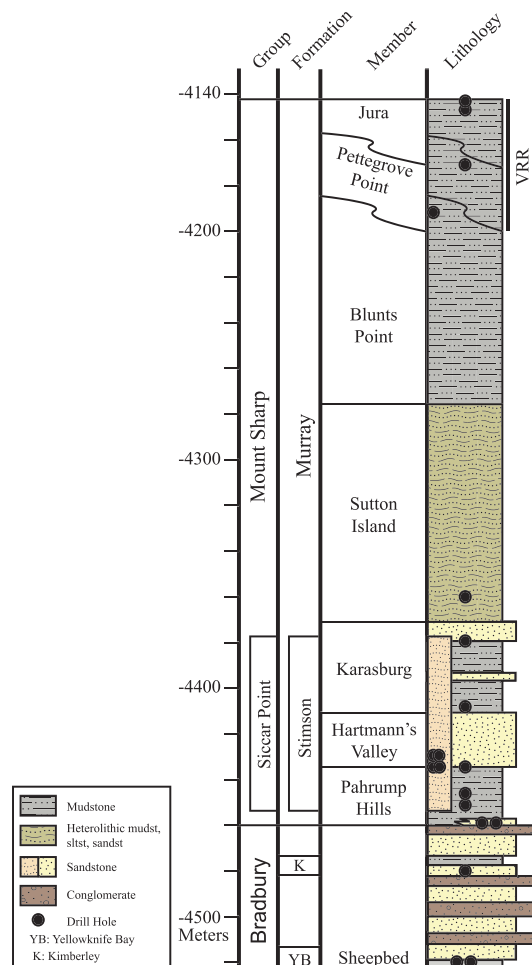


**Figure 2.** Stratigraphy column covering the traverse of the Curiosity rover from the landing in the Bradbury group and subsequent traverse into the Mount Sharp group and up Mount Sharp (modified from Fedo et al., 2019). The stratigraphic interval of VRR has been annotated.

et al., 2017). The drill sample collected at the Marias Pass location in the Pahrump Hills member (Figure 1b) contains abundant tridymite, which is interpreted as detrital and provides evidence for silicic volcanism on Mars (Morris et al., 2016). In the same stratigraphic interval, evidence for substantial diagenetic activity was observed in the form of light-toned, fracture-associated halos in Murray formation bedrock and in the unconformably overlying Stimson formation, suggesting late-stage diagenetic alteration (Frydenvang et al., 2017; Yen et al., 2017). Throughout this interval, the SiO<sub>2</sub> content in Murray formation bedrock is substantially elevated relative to Murray formation bedrock overall. Observation points from this section have been designated as a separate “Marias Pass class” here.

### 2.1. Observations on VRR

Based on the in situ observations acquired as part of the VRR campaign (Edgar et al., 2020; Fraeman, Johnson, et al., 2020; Stein et al., 2020), the ridge predominantly comprises laminated mudstone, similar to the lithologies observed in the underlying members of the Murray formation. While VRR was mapped as a distinct unit using data from orbital platforms (Anderson & Bell, 2010; Fraeman et al., 2016), the VRR campaign recognized that the ridge-forming rocks are stratigraphically part of the Murray formation and are divided into the Pettegrove Point and overlying Jura members of the Murray formation (Edgar et al., 2020; Fraeman, Catalano, et al., 2020). These observations imply that the Murray formation, extending vertically from the Pahrump Hills location and through VRR (Figures 1b and 2), is more than 350 m thick. Observations acquired upon entering the Glen Torridon area south of VRR show that the rocks just south of VRR likewise belong to the Jura member of the Murray formation (Fedo et al., 2020; Stein et al., 2020). Observation points from the Glen Torridon area will, however, be designated as belonging to a “Glen Torridon” class here to avoid confusion with the Jura member observations on VRR.

One noteworthy observation that arises from the detailed lateral studies of the member contacts enabled by the VRR campaign is that the contacts between the Blunts Point, Pettegrove Point, and Jura members are encountered at different elevations along the two traverses across VRR (Edgar et al., 2020). What drives the change in contact elevation is not clear from the stratigraphic investigations; specifically, in situ outcrop observations at VRR indicate that dips are subhorizontal (Stein et al., 2020).

Another notable feature of VRR bedrock is the presence of areas of gray coloration that are spectrally distinct from the more ubiquitous reddish colored rocks that otherwise define the rocks exposed on VRR (Edgar et al., 2020; Fraeman, Johnson, et al., 2020; Horgan et al., 2019; L’Haridon et al., 2020). Patches with gray rocks are primarily observed in the Jura member but are also observed in the Pettegrove Point member. Gray rocks are typically found in local topographic depressions, but contacts between red and gray rocks cut across primary layering (Edgar et al., 2020; Fraeman, Johnson, et al., 2020). These distinct patches of gray-toned rocks represent another subdivision acknowledged in the ChemCam data classification as “gray” classes of Jura and Pettegrove Point members (Figure 1b).

A total of three drilled samples were successfully acquired on VRR and one immediately below the ridge. Several additional drill attempts were also made where the rock proved too hard for Curiosity to drill (all are annotated in Figure S1 in the supporting information). The goal for the drill activities (see Fraeman, Catalano, et al., 2020; McAdam et al., 2020; Rampe et al., 2020) was to investigate changes in mineralogy

and composition across VRR by sampling the Blunts Point member below the ridge (“Duluth”), the Pettegrove Point member (“Stoer”), and both red (“Rock Hall”) and gray (“Highfield”) rocks from the Jura member.

### 3. Methods and Observation Point Classification

#### 3.1. ChemCam Measurements

The ChemCam instrument on the Curiosity rover is a combined laser-induced breakdown spectroscopy (LIBS) instrument and coaligned Remote Micro-Imager (RMI) camera (Maurice et al., 2012; Wiens et al., 2012).

The RMI provides an optical resolution of  $\sim 40\text{--}50\ \mu\text{rad}$  (Maurice et al., 2012; Mouélic et al., 2015), making it the highest-resolution remote sensing camera on the Curiosity rover. The intent of the RMI is to provide crucial spatial context for each ChemCam LIBS observation point. Because the RMI is a black and white camera only, and to provide a wider spatial context, a Mastcam (Malin et al., 2017) color documentation image is typically also acquired of each ChemCam target.

A LIBS measurement is performed by firing a short and intense laser pulse that heats a small area of the target to several thousand Kelvin, creating a weakly ionized plasma. As the excited atoms and ions subsequently cool in  $\sim 1\ \mu\text{s}$ , light that is diagnostic of the atomic species present in the plasma is emitted as electrons relax to lower electronic states. By interpreting the strength and wavelength of the resulting emission lines, it is possible to identify which atoms are present in the sample and quantify the concentration of major elements (Clegg et al., 2017; Wiens et al., 2013) and select minor elements (Ollila et al., 2014; Payré et al., 2017).

Here, the bedrock composition of the major oxides ( $\text{SiO}_2$ ,  $\text{TiO}_2$ ,  $\text{Al}_2\text{O}_3$ ,  $\text{FeO}_T$ ,  $\text{MgO}$ ,  $\text{CaO}$ ,  $\text{Na}_2\text{O}$ , and  $\text{K}_2\text{O}$ ) and some minor elements (Li and Rb) are reported for all Murray bedrock up to and including VRR bedrock and targets from the first 13 sols after entering the subsequent Glen Torridon area (Figure 1). The Chemical Index of Alteration (CIA)—calculated as the molar ratio of  $\text{Al}_2\text{O}_3$  over the sum of  $\text{Al}_2\text{O}_3$ ,  $\text{CaO}$ ,  $\text{Na}_2\text{O}$ , and  $\text{K}_2\text{O}$  (Fedo et al., 1995; Nesbitt & Young, 1982)—is likewise presented based on the ChemCam major oxide measurements. Additionally, the normalized spectral line area of the main Mn emission lines in the 403- to 404-nm spectral window (normalized by total intensity of each spectrometer; see, e.g., Cousin et al., 2011; Lanza et al., 2014) is presented. While not quantitative, the normalized line intensity provides a robust qualitative measure of the relative Mn abundance. All geochemical data used in this paper are provided in Table S1 and are available, along with spectra of all points, via the NASA Planetary Data System (<http://pds-geosciences.wustl.edu/missions/msl/>). Anticipating that VRR would display high Fe content from the strong hematite spectral signatures observed from orbit, a dedicated verification of the iron calibration was developed (David et al., 2020). However, because the reported average  $\text{FeO}_T$  composition, except for a number of points on especially high-iron targets, is within the predictive range of the standard calibration used for ChemCam, all compositional data presented here are from the standard ChemCam quantitative calibration (Anderson et al., 2017; Clegg et al., 2017; Forni et al., 2013).

LIBS has a number of advantages that make it well suited for robotic planetary exploration, the most prominent of these being the combination of fast measurement times and the ability to perform standoff measurements. For ChemCam, geochemical analyses are routinely collected on Mars several meters from the rover, typically in the form of  $1 \times 5$ ,  $3 \times 3$ , or  $1 \times 10$  point observational raster configurations (Maurice et al., 2016), which have durations on the order of 20 min. This combination of speed and standoff capability enables ChemCam to probe the rover surroundings at most end-of-drive locations along the rover traverse, and as a result, more than 710,000 spectra have been downlinked from ChemCam on Mars (as of November 2019).

In addition to the speed and standoff capability of ChemCam, an important feature of ChemCam LIBS analyses is the ability of the generated laser-induced ablation to blow away dust that otherwise covers all rock surfaces on Mars. To account for the ubiquitous dust cover, which is observed in the first few shots of almost all ChemCam points (Maurice et al., 2016), the spectral processing of every recorded ChemCam spectrum (Wiens et al., 2013) discards the first five shots of the 30 shots (typically) on each observation point. This



ability of LIBS—and associated spectral processing—means that the reported ChemCam geochemical compositions represent dust-free surface compositions.

### 3.2. ChemCam Geochemistry Measurements and Point Classification

ChemCam provides an observation footprint with an equivalent diameter between 350 and 550  $\mu\text{m}$  (Maurice et al., 2012, 2016). This footprint is large compared to the very fine sand or smaller grain sizes that comprise most of the Murray formation (Fedozzi et al., 2019; Mangold et al., 2019; Rivera-Hernández et al., 2019, 2020) and implies that even compositions deduced from individual ChemCam observation points may be representative of the bulk rock composition. However, the ChemCam footprint is small compared to the approximately 1.6-cm diameter footprint of the APXS instrument (Campbell et al., 2012; Gellert & Clark, 2015), and importantly, it enables finer-scale differentiation between points on bedrock versus points on veins and other diagenetic features (see, e.g., L'Haridon et al., 2018; Nachon et al., 2014, 2017). This differentiation is facilitated by classification of each ChemCam observation point based primarily on the accompanying RMI and Mastcam documentation images.

The goal of the observation point classification is to identify observations that reflect the geochemistry of *bulk* bedrock from the stratigraphic members that compose the Murray formation (Figure 2). Here, *bulk* refers to observation points that are representative of the local bedrock geochemistry without later-stage localized diagenetic features. The point classification is primarily based on careful examination of associated context images, which enables identification of Ca-sulfate veins (Nachon et al., 2014, 2017) as well as concretions and/or layers that differ from the surrounding bedrock (Meslin et al., 2018; Rapin et al., 2019; Sun et al., 2018). In addition to visual inspection, the recorded geochemistry of each point is also used to support the point classification. Specifically, observation points showing a geochemistry that is considerably outside the range observed in neighboring observation points in the same raster and nearby targets are not counted as representative of the bulk bedrock geochemistry. Such *singular* points likely represent diagenetic cements and/or rare large grains that were hit within that location. To avoid inappropriately affecting the investigation of bulk geochemistry, the identification of such singular points is done conservatively. Apart from the ubiquitous Ca-sulfate veins and inclusions, which are noted as singular points showing high Ca, singular points should be rare compared to the identified bulk bedrock geochemistry. Outside of Ca-points and the high/low Fe-points on VRR detailed below, 2.3% of the Murray observation points are excluded as singular points (see Table S2 for details).

In addition to the point curation and to ensure the completeness of the reported geochemistry, all observation points on bedrock with a total sum of oxides less than 90 wt.% were discarded. ChemCam abundances are not renormalized to 100% and thus are not volatile free. A low total sum of oxides generally suggests the presence of elements not quantified by ChemCam; for example, points hitting Ca-sulfate typically display a low total sum of oxides as sulfur is not routinely quantified by ChemCam. Similarly, to ensure the quality of the reported geochemistry, only observation points closer than 3.5 m from the ChemCam instrument are included in the analyses presented here. Finally, specifically for gray Jura bedrock on VRR, it proved necessary to utilize  $\text{FeO}_T$  abundance as a discriminator between the bulk composition and low-Fe diagenetic features because a smooth transition is observed between the two with respect to both color and geochemistry.

### 3.3. Accuracy and Precision of Curated Data Set

The accuracy of the element quantification as identified by the calibration efforts of the ChemCam team (Clegg et al., 2017; Wiens et al., 2013), in addition to the standard deviation observed over the individual shots at each observation point, is provided in Table S1. The noted accuracy (root mean squared error of prediction) is calculated for the diverse calibration data set used to generate the quantification model for ChemCam geochemical observations (Clegg et al., 2017). In the chemostratigraphy plots presented (Figures 3–5), this accuracy is represented by a black bar underneath each plot, though not for Mn as we do not present quantitative predictions. For the reported CIA, the noted accuracy represents the linearly propagated error (Ku, 1966). For Murray formation bedrock observations, the spread of observation points around the average at a given elevation (Figures 3 and 4) is considered to be an upper limit to the actual relative precision between Murray formation observations, as the observed spread is due to both heterogeneities



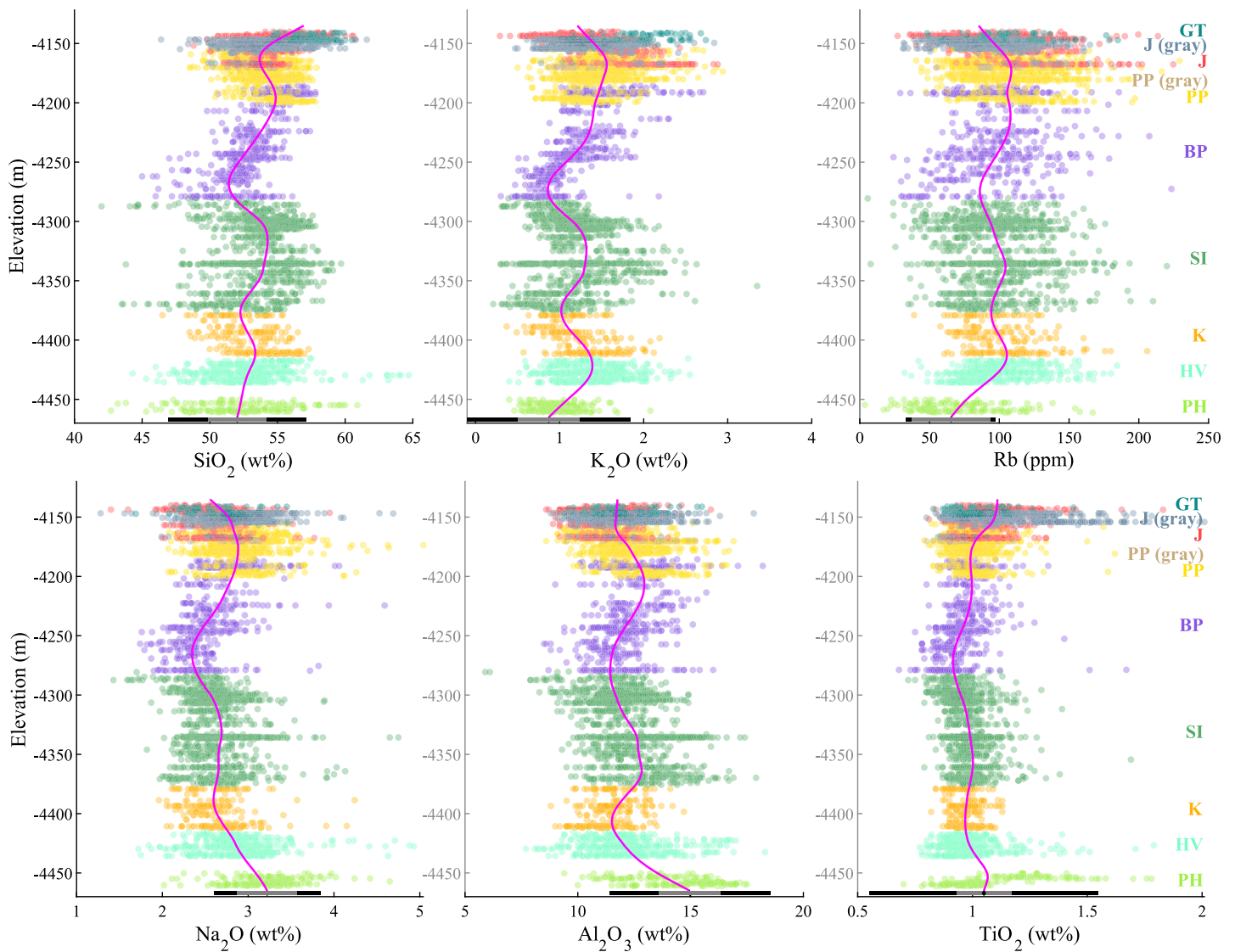


**Figure 3.** Geochemistry of individual ChemCam observation points plotted against elevation relative to the Martian datum for:  $\text{SiO}_2$ ,  $\text{K}_2\text{O}$ , Rb,  $\text{Na}_2\text{O}$ ,  $\text{Al}_2\text{O}_3$ , and  $\text{TiO}_2$ . The magenta line represents a smoothing spline fitted to the plotted data. The black bar represents the mean absolute accuracy for all observation points as noted in Table S1; the gray bar represents the relative precision between Murray bedrock targets; see section 3.3. The annotated classes are as follows: PH = Pahrump Hills; HV = Hartmann’s Valley; K = Karasburg; SI = Sutton Island; BP = Blunts Point; PP = Pettegrove Point; J = Jura; and GT = Glen Torridon. For J and PP, distinct classes of gray rocks are also annotated. Vera Rubin ridge comprises bedrock from the Pettegrove Point and Jura members.

within the bedrock and the precision of the measurement. This measure is approximated by a gray bar representing the root mean squared error of the spline fitted to the data.

### 3.4. Software and Data Analysis

The chemostratigraphy plots presented here were made using Matlab (2019a - update 2; The MathWorks, Inc.) and the plotted smoothing spline was generated using the Matlab “fit” function using the “smoothingspline” fit model with “SmoothingParam” set to  $1.0 \times 10^{-5}$  for all chemostratigraphy plots. The maps showing ChemCam targets were generated using Python 3.7.4 (Python Software Foundation, available at <http://www.python.org>) using the packages basemap, geopandas, shapely, rasterio, matplotlib, and pyproj—all acquired using the Anaconda Distribution (available at <http://www.anaconda.com>). The basemaps used were generated as detailed in Calef and Parker (2016). Data handling and management were performed in Microsoft Excel (version 16.29.1) and Python 3.7.4 using the numpy and pandas packages acquired using the Anaconda Distribution (available at <http://www.anaconda.com>).

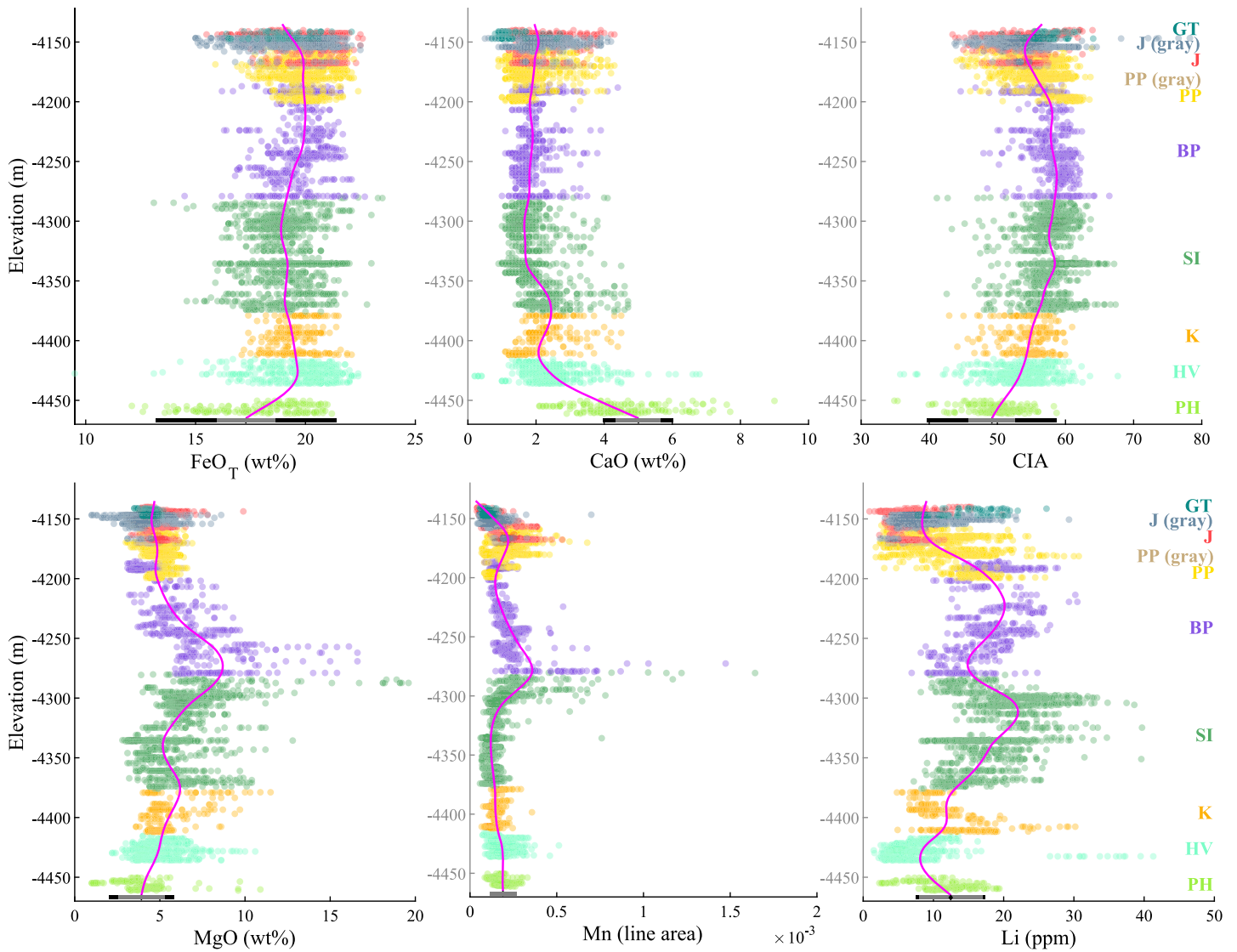


**Figure 4.** Geochemistry of individual ChemCam observation points plotted against elevation relative to the Martian datum for: FeOT, CaO, MgO, Mn, Li, and the Chemical Index of Alteration (CIA). The magenta line represents a smoothing spline fitted to the plotted data. The black bar represents the mean absolute accuracy for all observation points as noted in Table S1; the gray bar represents the relative precision between Murray bedrock targets; see section 3.3 for details. The annotated classes are as follows: PH = Pahrump Hills; HV = Hartmann's Valley; K = Karasburg; SI = Sutton Island; BP = Blunts Point; PP = Pettegrove Point; J = Jura; and GT = Glen Torridon. For J and PP, distinct classes of gray rocks are also annotated. Vera Rubin ridge comprises bedrock from the Pettegrove Point and Jura members.

## 4. Results

One key result from the VRR campaign was the similarity of VRR to underlying Murray formation bedrock. To reflect this, ChemCam observations going back to the first encounter of Murray formation bedrock at the Pahrump Hills location (Figure 1) are presented here to provide proper context for the subsequent VRR observations. All observation points that reflect Murray formation bulk geochemistry have been associated with the stratigraphic member where they were collected (Figures 1b and 2) and are reported in Table S1. Throughout section 4.1, we refer continuously to the Murray formation chemostratigraphy plotted in Figures 3 and 4.

### 4.1. Murray Formation Chemostratigraphy

With regards to major element composition, the Murray formation is relatively geochemically homogeneous across the more than 350-m-thick succession probed by the Curiosity rover from Pahrump Hills and into the

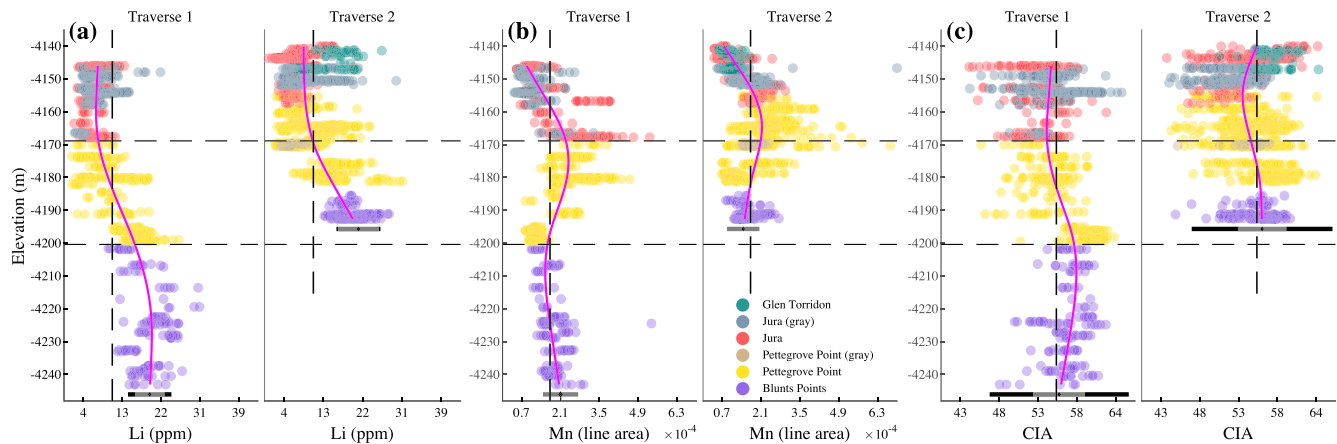


**Figure 5.** Variations in (a) Li abundance, (b) qualitative Mn content, and (c) CIA value plotted against elevation relative to the Martian datum along the two independent traverses of VRR from the Blunts Point member below the ridge to Jura at the top of the ridge, and including the descent into the Glen Torridon area on the second traverse (Figures 1c and 1d). Observation points hitting distinct gray rocks are annotated separately. On each plot, the vertical dashed line represents the mean value from the first traverse, also plotted on the second traverse to highlight the comparable levels along both traverses. Comparably, the horizontal dashed lines represent the contacts between Blunts Point and Pettegrove Point and Pettegrove Point and Jura members as observed on the first traverse, highlighting how the observed contact between members change in elevation on the ridge. The black bar represents the mean absolute accuracy for all observation points as noted in Table S1; the gray bar represents the relative precision between Murray bedrock targets; see section 3.3 for details. The magenta line is a smoothing spline fitted to the data in each subplot using same parameters as used for the full Murray chemostratigraphy (Figures 3 and 4).

Glen Torridon area south of VRR (Figures 1 and 2). That said, notable systematic variations occur within and across members of the Murray formation when viewed against elevation.

An important exception, however, to the Murray formation being geochemically homogenous is the Marias Pass class (sol 992–1110), which represents an end member for the Murray formation both geochemically and mineralogically (Frydenvang et al., 2017; Morris et al., 2016). Within the Marias Pass class, very high silica abundances are observed—with other oxide abundances mostly depleted. As it is not possible to deconvolve the detrital and diagenetic contributions to the Marias Pass composition and seeing that this unique class obscures other geochemical variations, it is deemed proper to exclude it from this analysis. The Murray formation chemostratigraphy including the Marias Pass class is shown in Figures S2 and S3 for reference.

Fitting a smoothing spline to the plotted ChemCam observation points provides a measure to track the large-scale chemostratigraphic variations up the Murray formation. By comparing the evolution of these splines for different elements, their stratigraphic correlation can be quantified by calculating the correlation coefficient between splines, regardless of whether any point-to-point correlation exists (Table S3). From this, a stratigraphic correlation is seen between  $\text{SiO}_2$ ,  $\text{K}_2\text{O}$ , and Rb. Conversely, the chemostratigraphic evolution of  $\text{FeO}_T$  does not correlate stratigraphically with elements other than Rb. Perhaps more importantly, the smoothing spline provides an easier visualization of bulk rock compositional variations than the point clouds. In particular, the correlation between  $\text{SiO}_2$ ,  $\text{K}_2\text{O}$ , and Rb can be confirmed by visual comparison, but the correlation breaks down on VRR as  $\text{SiO}_2$  abundance decreases, whereas  $\text{K}_2\text{O}$  and Rb abundances increase. Similarly, comparisons between the  $\text{FeO}_T$  and Rb plots reveal that the stratigraphic correlation is driven by a shared increase from Pahrump Hills to Hartmann's Valley.

The Pahrump Hills member, even when excluding the Marias Pass class, stands out as having a different composition than the rest of the Murray formation rocks. In particular, the CaO abundance drops when transitioning from the Pahrump Hills and into the overlying members, whereas the  $\text{FeO}_T$  abundance increases. Above the Pahrump Hills member, both elements are seen to be relatively constant. The  $\text{FeO}_T$  abundance is  $18.9 \text{ wt.}\% \pm 3.0 \text{ wt.}\%$  ( $1\sigma$ ) on average in this section, and the CaO content is  $2.0 \text{ wt.}\% \pm 0.7 \text{ wt.}\%$  on average (see also Mangold et al., 2019).

The abundances of Mn and MgO increase at the contact between the Sutton Island and Blunts Point members. For both elements, the abundances seen in this range represent a geochemical end member for the



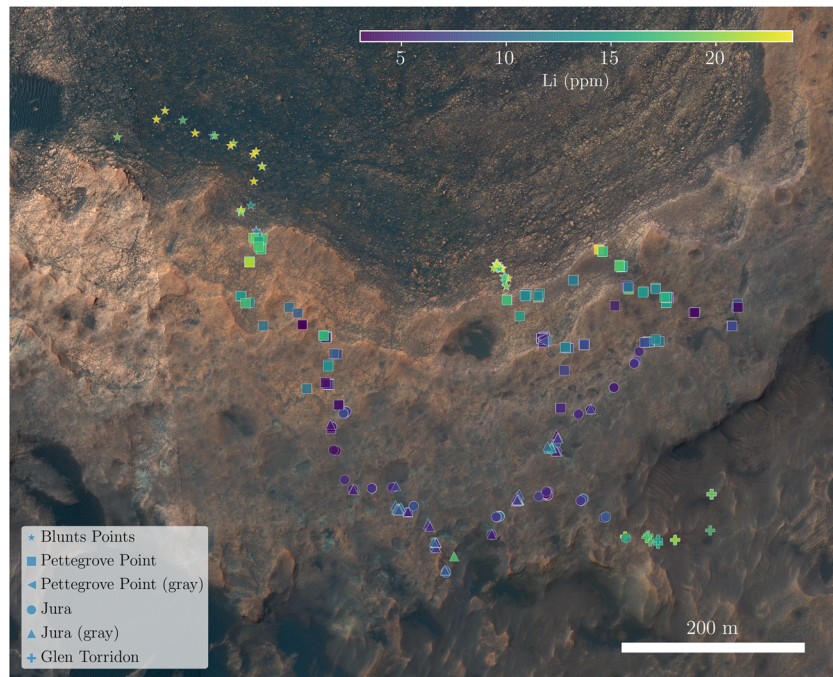


**Figure 6.** ChemCam observation points plotted on HiRISE mosaic showing the Vera Rubin ridge in Gale crater (Calef & Parker, 2016). Color code shows median Li content of bedrock point in each ChemCam target acquired on the ridge. A distinct decrease in Li abundance is observed up the northern slopes of VRR. Upon descending into the Glen Torridon area to the south, Li abundance increases to pre-VRR levels.

Murray formation and a high stratigraphic correlation between these is likewise noted. However, despite the stratigraphic correlation, no point-to-point correlation is observed between MgO and Mn content in this stratigraphic section (Figure S4). Importantly, for Mn, another notable, though not as strong, enrichment relative to the baseline level in the Murray formation is observed in the members that constitute VRR.

Whereas Mn and MgO are enriched at the contact between the Blunts Point and Sutton Island members, SiO<sub>2</sub>, K<sub>2</sub>O, Na<sub>2</sub>O Al<sub>2</sub>O<sub>3</sub>, TiO<sub>2</sub>, Li, and Rb all show a discernible decrease (as reflected by the fitted spline) in the same stratigraphic interval. This shared decrease at the contact between the Blunts Point and Sutton Island members is likely what is reflected in the observed positive chemostratigraphic correlation between Na<sub>2</sub>O and TiO<sub>2</sub> as well as Na<sub>2</sub>O and Al<sub>2</sub>O<sub>3</sub>, and not least in the negative correlation observed between SiO<sub>2</sub>, K<sub>2</sub>O, Na<sub>2</sub>O, and TiO<sub>2</sub> and MgO and to a lesser degree Mn (Table S3). Overall, the variations observed for Na<sub>2</sub>O, TiO<sub>2</sub>, and Al<sub>2</sub>O<sub>3</sub> are small relative to the observed point spread, though both Na<sub>2</sub>O and Al<sub>2</sub>O<sub>3</sub> are enriched in the Pahrump Hills member relative to the Murray formation overall. Furthermore, in gray Jura bedrock, TiO<sub>2</sub> appears enriched for some points, and some points in the same class show a depletion of FeO<sub>T</sub>.

The Li abundance is observed to increase overall with elevation for ~150 m up through the Murray formation, reaching a maximum in the upper half of the Sutton Island member. While the aforementioned local minimum is observed at the contact between the Sutton Island and Blunts Point members, Li remains at an elevated level up to VRR. While observation points from different members are cluttered in the plot, the Li abundance decreases across VRR, descending back down to the lowest levels observed in the Murray formation. Comparable to Li, as previously noted in (Mangold et al., 2019), the CIA increases up through the Murray formation from the Pahrump Hills member and up to the Blunts Point member. The CIA value does not show any decrease at the contact between the Blunts Point and Sutton Island members, but rather remains at an approximately constant level in the Blunts Point member. Upon reaching VRR, however, the CIA value decreases across VRR similar to the decrease in Li. The decrease in CIA appears to be caused by an apparent, though individually small, increase in Na<sub>2</sub>O and K<sub>2</sub>O across the Pettegrove Point member, associated with a drop in Al<sub>2</sub>O<sub>3</sub>. Additionally, it appears that both Li and CIA increase



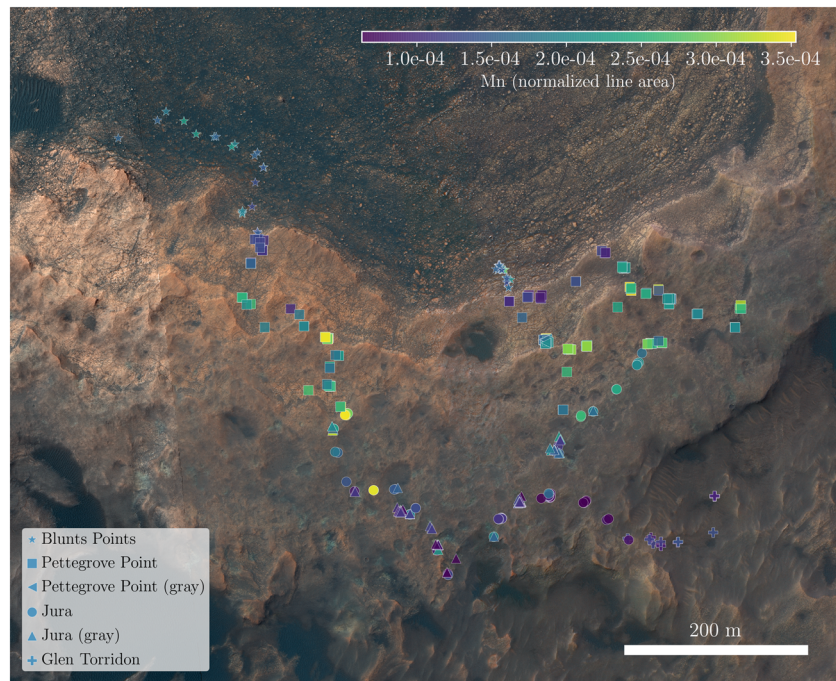


**Figure 7.** ChemCam observation points plotted on HiRISE mosaic showing the Vera Rubin ridge in Gale crater (Calef & Parker, 2016). Color code shows median Mn normalized line area value of bedrock point in each ChemCam target acquired on the ridge. A notable enrichment in Mn abundance is observed near the top of VRR, though not at the top. Comparing to Figure 6, the Mn enrichment occurs where the Li abundance has decreased to the low level seen across the Jura member.

upon entering the Glen Torridon area. From the similarity in evolution up through the Murray formation, the stratigraphic evolution of CIA versus Li is likewise correlated (Table S3).

#### 4.2. Geochemical Variations Observed on VRR

While some outliers are observed on the ridge even in the curated data set presented here, the plotted data (as traced by the fitted spline) show that most major and minor element abundances across VRR are overall within the compositional ranges of the Murray formation below the ridge (Figures 3 and 4). Nevertheless, notable overall decreases in Li and CIA and an enrichment in Mn are observed on the ridge. These variations are not outside the range previously observed in the Murray formation, but show a consistent trend across the ridge, and reflect a prominent shift relative to the chemostratigraphic evolution of the Murray formation.

To better visualize and understand the variations in Li, CIA, and Mn, observations from the two laterally separated transects of the ridge (Figures 1c and 1d) are plotted separately (Figure 5). From these, a similar compositional evolution is tracked along both transects going from the Blunts Point member and up through the Jura member. Importantly, the chemical evolution along each traverse does not follow elevation but does show a comparable trend across the lithologically defined members for both traverses. This is well expressed for the Li chemostratigraphy on VRR (Figure 5a): Along both transects, the Blunts Point member observations show a similar Li content (~15–20 ppm), a strong decrease is observed across the Pettegrove Point member, and the Jura member displays a constant low Li abundance (~5 ppm). As the rover descended into the Glen Torridon area south of VRR, the Li abundance increased to a level similar to that seen in the Blunts Point member. Similar to Li, though less prominent, CIA (Figure 5c) displays a decreasing trend across VRR that tracks the identified members rather than elevation, from ~58 in Blunts Point to ~54 in the Jura member. Also similar to the evolution of Li, as the rover descended into the Glen Torridon area, the CIA increased to ~58, similar to that observed in the Blunts Point member below VRR, though it appears that an elevated CIA is also found in the uppermost Jura member observations (Figure 5c).

For Mn, a different evolution than CIA and Li is observed (Figure 5b). The Mn abundance in the Blunts Point and lower Pettegrove Point members is similar to the baseline level seen in the Murray formation overall (Figure 4). At, or immediately below, the contact between the Pettegrove Point and Jura members, a substantial enrichment is observed along both traverses. Above the enrichment, in the Jura member, the Mn abundance returns to very low levels, potentially even lower than the baseline level seen in the Murray formation overall. While different from Li and CIA, the trends of Li, CIA, and Mn do, however, appear associated: Comparing the stratigraphic evolution of Mn to that of Li and CIA (Figure 5), Mn is enriched in the interval right above where both Li and CIA decrease along each traverse.

Plotted spatially rather than against elevation (Figures 6 and 7), Li abundance decreases going up the northern flank of the ridge (corresponding to the Pettegrove Point member) and reaches a steady low level across the top of the ridge (corresponding to Jura member). Notably, once the rover drove off the ridge to the south and entered the Glen Torridon area (lower portion of Figure 6), the Li abundance increases again to the level observed below VRR. Comparing Figures 6 and 7, the latter showing the qualitative evolution of Mn abundance, the observed enrichment in Mn appears to occur when Li has almost decreased to the low level seen in the Jura member.

From the spatial plots of geochemical variabilities, a distinct geochemical trend tracing the southern edge of VRR also emerges from the ChemCam data. In particular, an increase in the SiO<sub>2</sub> content is seen along the southern edge of VRR, continuing into the Glen Torridon area (Figure S1). Less noticeable, the CIA (unlike Li) also shows a slight increase along the southern edge of VRR (Figure S8). For individual targets, the increase is not unusual for VRR as a whole; indeed, other individual targets with elevated SiO<sub>2</sub> content are seen sporadically on the ridge, but the systematic increase across targets along the southern edge is notable. Importantly, this distinct zone with increased SiO<sub>2</sub> and CIA appears to include the Rock Hall drill sample (Figures S1 and S8). The APXS instrument reports a decrease in SiO<sub>2</sub> abundance for the Rock Hall drill area (Thompson et al., 2019), but since a substantial number of ChemCam points showing likely Ca-sulfate inclusions had to be excluded at and near the Rock Hall drill hole (Table S1), this APXS SiO<sub>2</sub> decrease could be caused by increased Ca sulfates within the APXS observational footprint.

#### 4.3. Gray Rocks on VRR

In addition to the observed chemostratigraphic variations observed on VRR, one of the prominent features of VRR is the presence of gray patches of rock in the Jura (primarily) and Pettegrove Point members that contrasts with the otherwise red-toned rocks on the ridge (Edgar et al., 2020; Fraeman, Johnson, et al., 2020; Horgan et al., 2019). In addition to the difference in color, a key feature of the gray rocks is the presence of abundant, subcentimeter dark-toned concretions with a very high (to pure) FeO<sub>T</sub> abundance (David et al., 2020; L'Haridon et al., 2020). Surrounding these high-iron concretions are lighter-toned “zones” that are conversely depleted in FeO<sub>T</sub> (see L'Haridon et al., 2020 for details).

Most gray patches are found in the Jura member, which therefore provides the best measure of comparison between red and gray bulk observations and observation points in the Jura member showing high and low Fe, respectively. The high-Fe class observations are found in identifiable dark concretions in gray bedrock primarily (Table S2); however, a smooth transition is observed between the lighter-toned low-Fe zones that typically surround the dark concretions and into the bulk gray bedrock (L'Haridon et al., 2020) (Figure S5). For this work, the smooth transition necessitated the use of 15 wt.% FeO<sub>T</sub> as a discriminator between bulk gray Jura rocks ( $19.3 \pm 1.6$  wt.% FeO<sub>T</sub>) and the low-Fe class. The low-Fe class tends to have slightly elevated SiO<sub>2</sub>, Al<sub>2</sub>O<sub>3</sub>, and Na<sub>2</sub>O relative to bulk Jura composition (Figure S6). Observation points in the high-Fe class are depleted in most other elements relative to Fe (David et al., 2020), the only exception being CaO and Mn (Figures S5 and S6). The elevated CaO abundance comes from the affinity of high-Fe nodules to Ca-sulfate veins (L'Haridon et al., 2020) and reflects that ChemCam observation points typically hit both Ca-sulfate and the high-Fe nodules. For Mn, while highly variable, the high-Fe class is overall enriched in Mn relative to the low-Fe class (L'Haridon et al., 2020) but not relative to the surrounding bulk gray Jura rocks—and hence also not enriched compared to the prominent Mn enrichment observed at the contact between the Pettegrove Point and Jura members (Figures 5 and S5). Outside of the high- and low-Fe Jura classes, the compositions of the bulk red and gray Jura bedrock are broadly similar (Figures S5 and S6). Gray Jura rocks appear to be slightly elevated in Na<sub>2</sub>O and depleted in MgO and Mn overall and have a larger fraction of

points showing elevated  $\text{TiO}_2$ , but a large overlap is observed. Additionally, a sampling bias appears to explain the apparent difference in Mn abundance between red and gray Jura rocks, as more red Jura bedrock was measured near the contact with the Pettegrove Point member where the Mn enrichment is observed (Figures 5b and S5). While not as evident, a similar sampling bias potentially also explains the other minor differences between red and gray Jura rocks (Figures 3–5 and S5–S7). If so, that would further underline the geochemical similarity between red and gray bulk rock. This observed similarity of red and gray Jura rocks differs from that reported by the APXS instrument (Thompson et al., 2019). APXS reports that gray Jura rocks show elevated  $\text{SiO}_2$  and  $\text{Al}_2\text{O}_3$  abundances relative to red Jura rocks (Thompson et al., 2019). As such, the trend observed by APXS in gray rocks relative to red rocks appear similar to the trend observed for the low-Fe points relative to bulk Jura by ChemCam (Figures S5 and S6), possibly suggesting that APXS observes a mix of these classes, but not the high-Fe concretions. The inherent uncertainties of the ChemCam and APXS quantification models could be the cause for this discrepancy.

## 5. Discussion

### 5.1. VRR in Relation to the Overall Murray Chemostratigraphy

Excluding exposures of Murray formation bedrock at the Marias Pass location, the chemostratigraphy of the Murray formation (Figures 3 and 4) remains broadly constant through the >350-m stratigraphy investigated in the MSL mission at the time of writing. This includes VRR, as the geochemistry of the rocks composing VRR does not stand out as an outlier relative to the Murray chemostratigraphy as a whole.

Systematic variations and stratigraphically related correlations are observed up through the Murray formation between a number of elements (Figures 3 and 4, Table S3). This variation in the geochemistry of the Murray formation has been interpreted either as the result of mixing of detrital sediments from of a number of distinct sediment source regions (Bedford et al., 2019) and/or the result of variation in degree of weathering of detrital components (Mangold et al., 2019). It is notable, however, that the stratigraphic correlation between Si, K, and Rb up through the Murray formation breaks down on VRR (Figure 3), which suggests that the VRR mudstones either had a differing provenance source or experienced a different postdepositional history relative to the underlying Murray formation.

Even when excluding the Marias Pass class for these analyses, the (lower) Pahrump Hills member stands out as a distinct geochemical end member in the Murray formation chemostratigraphy (Figures 3 and 4). Furthermore, no additional occurrences of the Marias Pass-like high-silica composition have been observed outside of the upper Pahrump Hills member, supporting the interpretation that this class reflects a distinct, temporally localized input to the lake basin (Morris et al., 2016) and later diagenesis (Frydenvang et al., 2017; Yen et al., 2017).

Above the Pahrump Hills member, another geochemical end member of the Murray chemostratigraphy is found at the contact between the Sutton Island and Blunts Point members. A strong enrichment in MgO and Mn is observed at this stratigraphic boundary and is associated with an apparent depletion in  $\text{SiO}_2$ ,  $\text{K}_2\text{O}$ ,  $\text{Na}_2\text{O}$ ,  $\text{Al}_2\text{O}_3$ ,  $\text{TiO}_2$ , Li, and Rb. Multiple hypotheses for the enrichment in MgO and Mn at this stratigraphic transition have been proposed, including authigenic formation in a lake margin environment or later diagenetic alteration (Gasda et al., 2019; Meslin et al., 2018; Rapin et al., 2019). For example, Rapin et al. (2019) observed apparent enrichments in S and H in conjunction with elevated Mg, found in several narrow stratigraphic windows containing rubbly bedrock, which they interpreted as being the result of formation in an evaporitic lake environment. Notably, outside distinct dark-toned layers also found in this stratigraphic interval that also display variable phosphorus abundances (Meslin et al., 2018), no joint enrichment of Mn and MgO is observed in ChemCam observation points. A hypothesis for the joint enrichment of these elements in the same stratigraphic interval is lacking at present. Sedimentary facies analyses of that section do not show compelling evidence for a strongly evaporitic environment (Fedo et al., 2019; Siebach et al., 2019) over larger scales than the few locations reported by Rapin et al. (2019).

On VRR, the overall bedrock geochemistry lies within the range observed in the Murray formation. Considering that VRR displays a stronger hematite spectral signature than surrounding Murray formation rocks as observed from orbit (Fraeman et al., 2013, 2016), it is notable that the mean  $\text{FeO}_T$  abundance does not increase in strata composing the VRR (Figure 4). The only prominent geochemical variations observed

on the ridge relative to the Murray chemostratigraphy overall are thus for Li, CIA, and Mn (Figures 3 and 4). For Mn, the enrichment observed on VRR is second only to the greater enrichment observed at the stratigraphic boundary between the Sutton Island and Blunts Point members. Lithium and CIA share the same behavior of decreasing up VRR, both decreasing to the similarly low level that was previously observed in the Hartmann's Valley member, ~275 m below VRR (Figure S9). Indeed, the Hartmann's Valley member as observed at the Oudam drill hole is geochemically similar to VRR for most elements (Figures 3 and 4).

## 5.2. Geochemical Variations Across VRR

It is notable that the geochemical variations in Li, CIA, and Mn observed within ridge strata do not follow elevation yet do follow the morphological expression of the ridge and show a consistent variation across the lithologically defined members (Figure 5).

While not a universal proxy for clay mineral content, terrestrial studies have shown a correlation between the clay mineral content of rocks and CIA values along with Li abundance. For CIA, the positive correlation with clay mineral content is inherent from the definition by Nesbitt and Young (1982) in its intended reflection of feldspar hydrolysis and concentration of aluminous clay mineral phases, although the CIA value is subject to modification during diagenesis (Fedó et al., 1995). While climatic and source region changes are observed to cause fluctuations in CIA values and may complicate interpretation on Earth, the correlation between CIA and clay mineral content has been identified at local to global scales (e.g., McLennan, 2000; Mischke & Zhang, 2010; Shao & Yang, 2012). On Mars, a tentative association of CIA and clay mineral abundance has been noted previously (Mangold et al., 2019; McLennan et al., 2014). Turning to lithium, on Earth, it concentrates in highly evolved igneous rocks (e.g., in pegmatites; Benson et al., 2017) but is highly susceptible to weathering (Starkey, 1982). Because of this, terrestrial studies have shown that Li is commonly found in the clay-size fraction of sediments (Starkey, 1982; Villumsen & Nielsen, 1976) and typically bound to clay minerals (Benson et al., 2017; Starkey, 1982; Vine, 1980). On Mars, the connection between Li and clay mineral abundance has likewise been indicated previously (Léveillé et al., 2014; McLennan et al., 2014).

The use of CIA and Li content as proxies for clay mineral content in Gale crater is overall consistent with drill sample mineralogy measurements from the CheMin instrument (Blake et al., 2012). An overall increase in clay mineral content was observed from the Pahrump Hills member up into the Sutton Island member (Bristow et al., 2018), which corresponds well with the overall increase in CIA (Mangold et al., 2019) and Li abundance (Figure 4). On VRR, a decrease in clay mineral content is likewise observed from the Duluth sample (~15 wt.%) below VRR in the Blunts Point member, to Stoer in the Pettegrove Point member (~10 wt.%), and a continued decrease to Highfield in the Jura member (~5 wt.%) (Rampe et al., 2020). However, the clay mineral content in the Rock Hall drill sample is higher, which does not accord with this hypothesis, as the Li abundance remains low in that area. However, the Rock Hall drill site lies within the “zone” along the southern edge of VRR that appears to show a subtle but distinct geochemistry from the rest of VRR, with elevated SiO<sub>2</sub> and CIA (Figures S1 and S8). As detailed below, we hypothesize that the southern edge of VRR has been affected by later/additional diagenetic processes relative to the rest of VRR.

Using CIA and Li as proxies for clay mineral content, it follows from the ChemCam data that the clay mineral content in VRR rocks likewise follows the morphology of the ridge rather than elevation and decreases strongly within the Pettegrove Point member (Figures 4 and 5). Furthermore, while it would be reasonable to suppose that the clay content of the rocks would be stratigraphically controlled, this appears not to be the case in that the clay content remains low in the Jura member rocks on VRR yet increases upon entering the Glen Torridon area south of VRR (Figures 5–7). ChemMin analysis of drill samples acquired immediately south of VRR in the Glen Torridon area (ChemCam data of this area not included here) confirmed the presence of elevated clay mineral abundance in the Glen Torridon Jura member rocks (Bristow et al., 2019; Thorpe et al., 2020). The approximately horizontal bedding and facies correlations between the Jura member rocks on VRR and in the Glen Torridon area south of VRR (Fedó et al., 2020; Stein et al., 2020) indicate a shared depositional history between these rock bodies. Despite the sedimentological similarity of stratigraphically equivalent rocks, we find that the low clay mineral content is specific to the rocks that constitute VRR.

The notable enrichment in Mn observed on VRR relative to the baseline level in the Murray formation is distinct from the geochemical variation observed for Li and CIA (Figures 5–7). From the inferred relation



between CIA and Li to clay mineral content, Mn is enriched right at or above the transition to low clay mineral content in the upper Pettegrove Point and Jura members. Above the interval enriched in Mn, the Mn level in Jura bedrock appears to be trending even lower than the baseline content in the Murray formation (Figures 4 and 5b). From the available observations, it is not possible to ascertain whether the Mn enrichment is detrital or diagenetic in nature and/or whether there is a causal relationship to the inferred decrease in clay mineral content observed immediately below the Mn enrichment along both traverses (Figure 5). One possible causal relationship could be that Mn was mobilized and migrated downwards until impeded by, possibly, rocks that are more impermeable due to their higher clay mineral content (Kamann et al., 2007). In such a scenario, the source for the Mn enrichment observed on VRR could be the overlying Jura rocks on VRR where an apparent slight depletion in Mn is observed. Alternatively, the interval enriched in Mn could be a detrital enrichment from the original deposition of the Murray formation. In such a scenario, the enrichment in Mn right above the decrease in clay content would be coincidental, and the change in elevation laterally along the ridge (Figure 5) could be a result of subsurface subsidence warping of both the enrichment in Mn as well as the member contacts.

Two additional observations from VRR stand out. One is the presence of the ubiquitous gray patches that crosscut stratigraphy in, predominantly, Jura member bedrock, but also seen in the Pettegrove Point member (see, e.g., Edgar et al., 2020; Fraeman, Johnson, et al., 2020; Horgan et al., 2019; Jacob et al., 2020). The other is the very notable subcentimeter-scale, dark-toned concretions of almost pure iron with Fe- and Mn-depleted zones around them observed in gray rocks (L'Haridon et al., 2020). This is interpreted as centimeter-scale Fe and Mn mobilization in the gray rocks on VRR (L'Haridon et al., 2020). Remarkably, despite the apparent small-scale Fe mobilization being a prominent feature of the gray patches of bedrock, little to no overall geochemical difference is observed between the bulk gray patches of rock and the more ubiquitous redder-toned rock of the Pettegrove Point and Jura member (Figures S5 and S6).

### 5.3. VRR Formation Scenarios

The data from the VRR campaign provide a number of key observations that any formation scenario for VRR has to address. This includes the presence of the ridge itself, prominently flanking the northwestern slope of Mt. Sharp (Figure 1a) and that the rocks composing VRR form part of the Murray formation. The geochemistry of the ridge adds to these observations, the first and foremost being the overall geochemical similarity to underlying Murray formation bedrock, including the lack of an overall enrichment in  $\text{FeO}_T$  despite the strong hematite spectral signature on the ridge observed from orbit. The overall similarity in bulk composition between red and gray rocks furthermore suggests that what caused the notable change in color did not lead to major bulk geochemical changes yet still led to centimeter-scale Fe and Mn mobilization in gray rocks. Despite the overall similarity, notable geochemical variations are observed across the ridge compared to the overall Murray chemostratigraphy. The first is the joint decrease in Li and CIA—*inferred to indicate clay mineral content*—across the Pettegrove Point member that cannot be explained via changes in depositional facies. The second is an enrichment in Mn just above the observed decrease in clay mineral content.

The mineralogy of the Highfield sample provides an additional constraint for any formation scenario. While the red-toned Stoer sample contains more hematite (~15 wt.%), the Highfield sample from gray Jura bedrock also contains a large fraction of hematite (~9 wt.%), which is *inferred to be gray hematite* due to the color of the rocks (Rampe et al., 2020). The formation of gray hematite is favored by temperatures above ambient (50–100°C) (Rampe et al., 2020) and high water-to-rock ratios (Turner et al., 2019). Modeling of the burial and diagenetic evolution of Gale sediment suggests that temperatures of the order of 50°C are possible for Murray rocks for most assumptions of thermal gradients, burial paths, and surface temperature conditions at the time when Murray rocks were deeply buried, and the rocks at VRR were covered by several hundreds of meters to a few kilometers of Mount Sharp rocks and eolian material (Borlina et al., 2015).

Hence, groundwater fluid circulation while the VRR rocks were deeply buried could have resulted in the dissolution of clays and the overall induration of the VRR rocks. The preferential formation of localized gray hematite over red hematite in some areas could be a result of locally elevated temperatures and/or greater water to rock ratio (Rampe et al., 2020; Turner et al., 2019) due to differences in permeability. In such a scenario, the observed enrichment of Mn would likely be a detrital input, and the formation of dark-toned high-

Fe concretions that are abundant in the gray rocks could be a result of later fluid interaction that likewise primarily affected the gray patches of bedrock due to their possibly greater permeability (L'Haridon et al., 2020). An open question for this scenario, however, is how such deep groundwater circulation would affect the VRR rocks specifically, resulting in a kilometer-long and 200-m-wide ridge flanking Mount Sharp (Figure 1a), yet not similarly affecting the Jura member strata in Glen Torridon just south of VRR. Groundwater could be channelized to affect VRR rocks specifically, for example, due to lateral variations in permeability from variations in grain size, but no such change was observed on VRR relative to lower lying Murray formation rocks (Edgar et al., 2020; Fedo et al., 2019).

Alternatively, the compelling similarity of the shape of the modern-day VRR and the Greenheugh pediment that unconformably drapes the Mount Sharp group (Anderson & Bell, 2010; Bryk et al., 2019; Malin & Edgett, 2000) to the south of VRR (Figure 1a) provides a possible control for why VRR formed where it did. Topographic studies suggest that the Greenheugh pediment, if it extended farther north, would precisely cap the top of modern-day VRR (Bryk et al., 2019). Fluids advancing underneath the Greenheugh pediment would thus preferentially interact with the rocks composing the modern-day VRR over the Jura member strata in Glen Torridon that would be buried deeper at this time. This scenario would place the relative timing of the fluid interaction long after the lake in Gale crater, after the burial and subsequent excavation of Gale to a paleosurface that exposed the Murray formation rocks, and after the paleosurface was buried again to form the draping Siccar Point group rocks (Banham et al., 2018; Fraeman et al., 2016; Frydenvang et al., 2017; Grotzinger et al., 2015). We do know from the previous discovery of fracture-related, high-silica halos in Stimson formation rocks (Frydenvang et al., 2017; Yen et al., 2017) that groundwater was relatively abundant even at this late time, but the presence of liquid above ambient temperatures becomes less clear at this stage. Unless Gale crater was substantially filled again as part of the deposition of the Siccar Point group, the source for elevated temperatures to preferentially form gray hematite (Rampe et al., 2020; Turner et al., 2019) remains unknown.

The latter scenario does, however, provide a possible framework for a causal relationship between the decrease in clay content on VRR and the enrichment in Mn in the stratigraphic interval right above—and not least to the small-scale Fe mobilization observed in gray rocks (L'Haridon et al., 2020). Both Mn and Fe are mobilized in a low pH fluid; however, low-pH alteration cannot explain the apparent preferential mobilization of Fe and Mn over other elements (Beitler et al., 2005). Alternatively, the solubilities of hematite and typical Mn minerals are highly redox sensitive compared to other typical minerals (Ardelan & Steinnes, 2010; Bonatti et al., 1971; Krauskopf, 1957; Lynn & Bonatti, 1965). In seafloor sediments, Mn is observed to be mobilized upwards toward the interface between the sediments and ocean water due to reducing conditions in the subsurface preferentially dissolving Mn, causing it to migrate upwards and eventually precipitating in the oxidizing top section that is in contact with the water (Ardelan & Steinnes, 2010; Bonatti et al., 1971; Fones et al., 2004; Lynn & Bonatti, 1965). More relatable to observations on VRR, redox-dependent dissolution and subsequent precipitation under oxidizing conditions are reported to be the cause of bleaching of red rocks on Earth where Fe and Mn are preferentially dissolved from rocks displaying distinct red color from the presence of hematite. The potential combination of larger-scale Mn mobilization and smaller-scale Fe mobilization on VRR could therefore potentially be explained by a reducing fluid advancing downwards under the Greenheugh pediment, preferentially dissolving Mn and Fe (Krauskopf, 1957). When mobilized, Fe reprecipitates easier than Mn under oxidizing conditions (Beitler et al., 2005; Chan et al., 2000; Eren et al., 2015; Krauskopf, 1957), and the presence of sulfates could induce the oxidation and reprecipitation of hematite as observed in the high-iron nodules in gray Jura rocks (L'Haridon et al., 2020). Mn would be mobilized further and only precipitate after, potentially, pooling on top of more impermeable rocks with higher clay mineral content in the lower Pettegrove Point.

The source for any reducing fluids is unknown in this framework, however, and no reduced mineral species are observed in the drill samples collected on VRR (Rampe et al., 2020). A possible reducing source could be sulfite-containing groundwater, as suggested by Wong et al. (2020) based on SAM (Mahaffy et al., 2012) analyses of the collected drill samples. Additionally, previous studies have inferred anoxic conditions in the deep parts of the ancient Gale crater lake where groundwater influx is decoupled from more oxidizing surface conditions, leading to reduced species being deposited (Hurowitz et al., 2017). In both cases, however, why we would not observe any reduced species today is unclear.

For both VRR formation scenarios outlined, it remains unclear, however, how it would be possible to dissolve clay minerals to the extent observed on the ridge yet leave the major element geochemistry mostly unchanged, unless the modern-day geochemistry is the result of multiple diagenetic events. The presence of akaganeite as the major Fe oxide in the Rock Hall sample, inferred to form in acidic saline fluids (Rampe et al., 2020), likewise suggests additional diagenetic alteration of the VRR rocks outside of that detailed in the formation scenarios above. This sample was drilled from the distinct geochemical zone along the southern edge of VRR (Figures S1 and S8) that appears to extend into the Glen Torridon area. As also suggested by modeling (Turner et al., 2019), this alteration might reflect a separate, later diagenetic event that is perhaps more reflective of the geological evolution of the Glen Torridon area south of VRR. Even so, it adds to a notion that the rocks composing VRR likely experienced multiple stages of fluid interaction.

## 6. Conclusions

From the observations acquired on VRR and along Curiosity's traverse up through the Murray formation stratigraphy, ChemCam data show that VRR is geochemically within the range of compositions previously observed in Murray formation bedrock. However, a notable decrease in Li content and CIA across the ridge is inferred to reflect a nonstratigraphically controlled decrease in clay mineral content. Just above the inferred decrease in clay mineral content, a prominent enrichment in Mn relative to baseline levels is observed. Within gray patches of rock found on VRR, abundant evidence of centimeter-scale Fe mobilization is observed (L'Haridon et al., 2020), yet the bulk composition of gray rocks is similar to that of the more ubiquitous red rocks.

No single process has been identified that can convincingly explain all the observations acquired as part of the VRR campaign, likely suggesting that the VRR rocks underwent multiple interactions with diagenetic fluids after the lacustrine deposition in Gale crater had ceased. Fluid interaction caused a pervasive dissolution of clay minerals in the upper Pettegrove Point and Jura member rocks of VRR. However, this did not occur in the stratigraphically equivalent Jura member rocks (Fedó et al., 2020; Stein et al., 2020) in the Glen Torridon area south of VRR. Fluid interaction likewise led to the patchy alteration of VRR sediment into red and gray rocks and their overall induration of VRR rocks, making them more erosionally resistant than the surrounding Murray formation bedrock. VRR thus emerged as a ridge through its greater relative erosional resistance. The origin of the Mn enrichment likewise remains unclear; it could reflect a detrital enrichment or be the result of mobilization by reducing fluids that potentially also explains the presence of small-scale Fe and Mn mobilization in gray rocks (L'Haridon et al., 2020). The source for such reducing fluids remains speculative.

The recognition that VRR rocks represent a continuation of the lacustrine Murray formation (Edgar et al., 2020; Fraeman, Catalano, et al., 2020) adds additional thickness to the Murray formation (>350 m total) and thus additional duration to the habitable environment that existed in the ancient Gale crater lake (Fedó et al., 2019; Grotzinger et al., 2015). It also implies that we have yet to find the geological record of a changing climate in Gale crater. This remains a key goal for the MSL mission as the Curiosity rover continues up Mount Sharp. The evidence for substantial late-stage interaction with groundwater in VRR rocks further highlights the persistence of groundwater long after the lacustrine environment in Gale crater ceased (Frydenvang et al., 2017; Gasda et al., 2017; Yen et al., 2017), likely further extending the duration of habitable environments in Gale crater.

## Data Availability Statement

All geochemical data used in this paper are provided in Table S1 and are available, along with spectra of all points, via the NASA Planetary Data System (<http://pds-geosciences.wustl.edu/missions/msl/>). Table S1 can also be acquired at [doi.org/10.17894/ucph.80bf74b2-c569-45f8-813e-0c70e44bf298](https://doi.org/10.17894/ucph.80bf74b2-c569-45f8-813e-0c70e44bf298). Any use of trade, firm, or product names is for descriptive purposes only and does not imply endorsement by the U.S. Government.

## References

- Anderson, R. B., & Bell, J. F. I. (2010). Geologic mapping and characterization of Gale Crater and implications for its potential as a Mars Science Laboratory landing site. *International Journal of Mars Science and Exploration*, 5(76), 128. <https://doi.org/10.1555/mars.2010.0004>

## Acknowledgments

This work was supported by the NASA MSL Mission—operated by the Jet Propulsion Laboratory, California Institute of Technology—and the NASA Mars Exploration Program. We acknowledge the support of the MSL engineering and operations staff. JF acknowledges the support of the Carlsberg Foundation. NM, JLH, OG, SM, and PYM acknowledge the support of CNES for their work on MSL ChemCam. CCB was funded through the STFC doctoral training grant to the OU. A portion of this research was carried out at the Jet Propulsion Laboratory, California Institute of Technology, under a contract with the National Aeronautics and Space Administration.

- Anderson, R. B., Clegg, S. M., Frydenvang, J., Wiens, R. C., McLennan, S., Morris, R. V., et al. (2017). Improved accuracy in quantitative laser-induced breakdown spectroscopy using sub-models. *Spectrochimica Acta Part B: Atomic Spectroscopy*, *129*(49), 49–57. <https://doi.org/10.1016/j.sab.2016.12.002>
- Ardelan, M. V., & Steinnes, E. (2010). Changes in mobility and solubility of the redox sensitive metals Fe, Mn and Co at the seawater-sediment interface following CO<sub>2</sub> seepage. *Biogeosciences*, *7*(2), 569–583. <https://doi.org/10.5194/bg-7-569-2010>
- Banham, S. G., Gupta, S., Rubin, D. M., Watkins, J. A., Sumner, D. Y., Edgett, K. S., et al. (2018). Ancient Martian aeolian processes and palaeomorphology reconstructed from the Stimson formation on the lower slope of Aeolis Mons, Gale Crater, Mars. *Sedimentology*, *65*(4), 993–1042. <https://doi.org/10.1111/sed.12469>
- Bedford, C. C., Bridges, J. C., Schwenzer, S. P., Wiens, R. C., Rampe, E. B., Frydenvang, J., & Gasda, P. J. (2019). Alteration trends and geochemical source region characteristics preserved in the fluviolacustrine sedimentary record of Gale Crater, Mars. *Geochimica et Cosmochimica Acta*, *246*, 234–266. <https://doi.org/10.1016/j.gca.2018.11.031>
- Bedford, C. C., Schwenzer, S. P., Bridges, J. C., Banham, S., Wiens, R. C., Gasnault, O., et al. (2020). Geochemical variation in the Stimson formation of Gale Crater: Provenance, mineral sorting, and a comparison with modern Martian dunes. *Icarus*, *341*, 113622. <https://doi.org/10.1016/j.icarus.2020.113622>
- Beitler, B., Parry, W. T., & Chan, M. A. (2005). Fingerprints of fluid flow: Chemical diagenetic history of the Jurassic Navajo Sandstone, Southern Utah, U.S.A. *Journal of Sedimentary Research*, *75*(4), 547–561. <https://doi.org/10.2110/jsr.2005.045>
- Benson, T. R., Coble, M. A., Rytuba, J. J., & Mahood, G. A. (2017). Lithium enrichment in intracontinental rhyolite magmas leads to Li deposits in caldera basins. *Nature Communications*, *8*(1), 1–9. <https://doi.org/10.1038/s41467-017-00234-y>
- Blake, D., Vaniman, D., Achilles, C., Anderson, R., Bish, D., Bristow, T., et al. (2012). Characterization and calibration of the CheMin mineralogical instrument on Mars Science Laboratory. *Space Science Reviews*, *170*(1–4), 341–399. <https://doi.org/10.1007/s11214-012-9905-1>
- Bonatti, E., Fisher, D. E., Joensuu, O., & Rydell, H. S. (1971). Postdepositional mobility of some transition elements, phosphorus, uranium and thorium in deep sea sediments. *Geochimica et Cosmochimica Acta*, *35*(2), 189–201. [https://doi.org/10.1016/0016-7037\(71\)90057-3](https://doi.org/10.1016/0016-7037(71)90057-3)
- Borlina, C. S., Ehlmann, B. L., & Kite, E. S. (2015). Modeling the thermal and physical evolution of Mount Sharp's sedimentary rocks, Gale Crater, Mars: Implications for diagenesis on the MSL Curiosity rover. *Journal of Geophysical Research: Planets*, *120*, 1396–1414. <https://doi.org/10.1002/2015JE004799>
- Bristow, T. F., Rampe, E. B., Grotzinger, J. P., Fox, V. K., Bennett, K. A., Yen, A. S., et al. (2019). *Clay minerals of Glen Torridon, Mount Sharp, Gale crater, Mars* (p. 6390). Paper presented at Ninth International Conference on Mars.
- Bristow, T. F., Rampe, E. B., Achilles, C. N., Blake, D. F., Chipera, S. J., Craig, P., et al. (2018). Clay mineral diversity and abundance in sedimentary rocks of Gale Crater, Mars. *Science Advances*, *4*(6), eaar3330. <https://doi.org/10.1126/sciadv.aar3330>
- Bryk, A. B., Dietrich, W. E., Lamb, M. P., Grotzinger, J. P., Vasavada, A. R., Stack, K. M., et al. (2019). *What was the original extent of the Greenheugh pediment and Gediz Vallis ridge deposits in Gale crater, Mars?* (p. 6296). Paper presented at Ninth International Conference on Mars.
- Calef, F., & Parker, T. (2016). MSL Gale merged orthophoto mosaic. PDS Annex, U.S. Geological Survey. [http://bit.ly/MSL\\_Basemap](http://bit.ly/MSL_Basemap)
- Campbell, J. L., Perrett, G. M., Gellert, R., Andrushenko, S. M., Boyd, N. I., Maxwell, J. A., et al. (2012). Calibration of the Mars Science Laboratory alpha particle X-ray spectrometer. *Space Science Reviews*, *170*(1–4), 319–340. <https://doi.org/10.1007/s11214-012-9873-5>
- Chan, M. A., Parry, W. T., & Bowman, J. R. (2000). Diagenetic hematite and manganese oxides and fault-related fluid flow in Jurassic sandstones, Southeastern Utah. *AAPG Bulletin*, *84*(9), 1281–1310. <https://doi.org/10.1306/a9673e82-1738-11d7-8645000102c1865d>
- Clegg, S. M., Wiens, R. C., Anderson, R., Forni, O., Frydenvang, J., Lasue, J., et al. (2017). Recalibration of the Mars Science Laboratory ChemCam instrument with an expanded geochemical database. *Spectrochimica Acta Part B: Atomic Spectroscopy*, *129*, 64–85. <https://doi.org/10.1016/j.sab.2016.12.003>
- Cousin, A., Forni, O., Maurice, S., Gasnault, O., Fabre, C., Sautter, V., et al. (2011). Laser induced breakdown spectroscopy library for the Martian environment. *Spectrochimica Acta Part B: Atomic Spectroscopy*, *66*(11–12), 805–814. <https://doi.org/10.1016/j.sab.2011.10.004>
- David, G., Cousin, A., Forni, O., Meslin, P.-Y., Dehouck, E., Mangold, N., et al. (2020). Analyses of high-iron sedimentary bedrock and diagenetic features observed with ChemCam at Vera Rubin ridge, Gale crater, Mars: Calibration and characterization. *Journal of Geophysical Research: Planets*, e2019JE006314. <https://doi.org/10.1029/2019JE006314>
- Edgar, L. A., Fedo, C. M., Gupta, S., Banham, S. G., Fraeman, A. A., Grotzinger, J. P., et al. (2020). A lacustrine paleoenvironment recorded at Vera Rubin ridge, Gale crater: Overview of the sedimentology and stratigraphy observed by the Mars Science Laboratory Curiosity Rover. *Journal of Geophysical Research: Planets*, *125*, e2019JE006307. <https://doi.org/10.1029/2019JE006307>
- Eren, M., Kadir, S., Kapur, S., Huggett, J., & Zucca, C. (2015). Colour origin of Tortonian red mudstones within the Mersin area, southern Turkey. *Sedimentary Geology*, *318*, 10–19. <https://doi.org/10.1016/j.sedgeo.2014.12.003>
- Fedo, C. M., Grotzinger, J. P., Bryk, A., Edgar, L. A., Bennett, K., Fox, V., et al. (2020). *Ground-based stratigraphic correlation of the Jura and Knockfarril Hill members of the Murray formation, Gale crater: Bridging the Vera Rubin ridge–Glen Torridon divide* (p. 2345). Paper presented at 51st Lunar and Planetary Science Conference.
- Fedo, C. M., Grotzinger, J. P., Gupta, S., Banham, S., Bennett, K., Edgar, L., et al. (2019). *Evidence for persistent, water-rich, lacustrine deposition preserved in the Murray formation, Gale crater: A depositional system suitable for sustained habitability* (p. 6308). Paper presented at Ninth International Conference on Mars.
- Fedo, C. M., Nesbitt, H. W., & Young, G. M. (1995). Unraveling the effects of potassium metasomatism in sedimentary rocks and paleosols, with implications for paleoweathering conditions and provenance. *Geology*, *23*(10), 921–924. [https://doi.org/10.1130/0091-7613\(1995\)023<0921:uteopm>2.3.co;2](https://doi.org/10.1130/0091-7613(1995)023<0921:uteopm>2.3.co;2)
- Fones, G. R., Davison, W., & Hamilton-Taylor, J. (2004). The fine-scale remobilization of metals in the surface sediment of the north-east Atlantic. *Continental Shelf Research*, *24*(13–14), 1485–1504. <https://doi.org/10.1016/j.csr.2004.05.007>
- Forni, O., Maurice, S., Gasnault, O., Wiens, R. C., Cousin, A., Clegg, S. M., et al. (2013). Independent component analysis classification of laser induced breakdown spectroscopy spectra. *Spectrochimica Acta Part B-Atomic Spectroscopy*, *86*(31), 31–41. <https://doi.org/10.1016/j.sab.2013.05.003>
- Fraeman, A. A., Arvidson, R. E., Catalano, J. G., Grotzinger, J. P., Morris, R. V., Murchie, S. L., et al. (2013). A hematite-bearing layer in Gale Crater, Mars: Mapping and implications for past aqueous conditions. *Geology*, *41*(10), 1103–1106. <https://doi.org/10.1130/g34613.1>
- Fraeman, A. A., Ehlmann, B. L., Arvidson, R. E., Edwards, C. S., Grotzinger, J. P., Milliken, R. E., et al. (2016). The stratigraphy and evolution of lower Mount Sharp from spectral, morphological, and thermophysical orbital data sets. *Journal of Geophysical Research: Planets*, *121*, 1713–1736. <https://doi.org/10.1002/2016JE005095>



- Fraeman, A. A., Edgar, L. A., Rampe, E. B., Thompson, L. M., Frydenvang, J., Fedo, C. M., et al. (2020). Evidence for a Diagenetic Origin of Vera Rubin Ridge, Gale Crater, Mars: Summary and Synthesis of Curiosity's Exploration Campaign. *Journal of Geophysical Research: Planets*, e2020JE006527. <https://doi.org/10.1029/2020JE006527>
- Fraeman, A. A., Johnson, J. R., Arvidson, R. E., Rice, M. S., Wellington, D. F., Morris, R. V., et al. (2020). Synergistic ground and orbital observations of iron oxides on Mt. Sharp and Vera Rubin ridge. *Journal of Geophysical Research: Planets*, e2019JE006294. <https://doi.org/10.1029/2019JE006294>
- Frydenvang, J., Gasda, P. J., Hurowitz, J. A., Grotzinger, J. P., Wiens, R. C., Newsom, H. E., et al. (2017). Diagenetic silica enrichment and late-stage groundwater activity in Gale Crater, Mars. *Geophysical Research Letters*, 44, 4716–4724. <https://doi.org/10.1002/2017GL073323>
- Gasda, P. J., Lanza, N., Meslin, P.-Y., Forni, O., L'Haridon, J., Fischer, W. W., et al. (2019). *High-Mn sandstone as evidence for oxidized conditions in Gale Crater Lake* (p. 1620). Paper presented at 50th Lunar and Planetary Science Conference.
- Gasda, P. J., Haldeman, E. B., Wiens, R. C., Rapin, W., Bristow, T. F., Bridges, J. C., et al. (2017). In situ detection of boron by ChemCam on Mars. *Geophysical Research Letters*, 44, 8739–8748. <https://doi.org/10.1002/2017GL074480>
- Gellert, R., & Clark, B. C. (2015). In situ compositional measurements of rocks and soils with the alpha particle X-ray spectrometer on NASA's Mars rovers. *Elements*, 11(1), 39–44. <https://doi.org/10.2113/gselements.11.1.39>
- Grotzinger, J. P., Gupta, S., Malin, M. C., Rubin, D. M., Schieber, J., Siebach, K., et al. (2015). Deposition, exhumation, and paleoclimate of an ancient lake deposit, Gale Crater, Mars. *Science*, 350(6257), aac7575. <https://doi.org/10.1126/science.aac7575>
- Grotzinger, J. P., & Milliken, R. E. (2012). The sedimentary rock record of Mars: Distribution, origins, and global stratigraphy. *SEPM Special Publication*, 102, 1–48. Print ISBN 978-1-56576-312-8
- Horgan, B., Fraeman, A. A., Johnson, J. R., Thompson, L. M., Jacob, S., Wellington, D., et al. (2019). Redox conditions during diagenesis in the Vera Rubin ridge, Gale Crater, Mars, from Mastcam multispectral images (p. 1424). Paper presented at 50th Lunar and Planetary Science Conference, The Woodlands, TX.
- Hurowitz, J. A., Grotzinger, J. P., Fischer, W. W., McLennan, S. M., Milliken, R. E., Stein, N., et al. (2017). Redox stratification of an ancient lake in Gale Crater, Mars. *Science*, 356(6341), eaah6849. <https://doi.org/10.1126/science.aah6849>
- Jacob, S. R., Wellington, D. F., Bell, J. F. III, Achilles, C., Fraeman, A. A., Horgan, B., Johnson, J. R., et al. (2020). Spectral, compositional, and physical properties of the Upper Murray Formation and Vera Rubin ridge, Gale crater, Mars. *Journal of Geophysical Research: Planets*. <https://doi.org/10.1029/2019JE006290>
- Kamann, P. J., Ritzi, R. W., Dominic, D. F., & Conrad, C. M. (2007). Porosity and permeability in sediment mixtures. *Groundwater*, 45(4), 429–438. <https://doi.org/10.1111/j.1745-6584.2007.00313.x>
- Krauskopf, K. B. (1957). Separation of manganese from iron in sedimentary processes. *Geochimica et Cosmochimica Acta*, 12(1–2), 61–84. [https://doi.org/10.1016/0016-7037\(57\)90018-2](https://doi.org/10.1016/0016-7037(57)90018-2)
- Ku, H. H. (1966). Notes on the use of propagation of error formulas. *Journal of Research of the National Bureau of Standards, Section C: Engineering and Instrumentation*, 70C(4), 263. <https://doi.org/10.6028/jres.070c.025>
- L'Haridon, J., Mangold, N., Fraeman, A. A., Johnson, J. R., Cousin, A., Rapin, W., et al. (2020). Iron mobility during diagenesis at Vera Rubin ridge, Gale Crater, Mars. *Journal of Geophysical Research: Planets*, 125, e2019JE006299. <https://doi.org/10.1029/2019JE006299>
- L'Haridon, J., Mangold, N., Meslin, P.-Y., Johnson, J. R., Rapin, W., Forni, O., et al. (2018). Chemical variability in mineralized veins observed by ChemCam on the lower slopes of Mount Sharp in Gale Crater, Mars. *Icarus*, 311, 69–86. <https://doi.org/10.1016/j.icarus.2018.01.028>
- Lanza, N. L., Fischer, W. W., Wiens, R. C., Grotzinger, J., Ollila, A. M., Cousin, A., et al. (2014). High manganese concentrations in rocks at Gale Crater, Mars. *Geophysical Research Letters*, 41, 5755–5763. <https://doi.org/10.1002/2014GL060329>
- Léveillé, R. J., Bridges, J., Wiens, R. C., Mangold, N., Cousin, A., Lanza, N., et al. (2014). Chemistry of fracture-filling raised ridges in Yellowknife Bay, Gale Crater: Window into past aqueous activity and habitability on Mars. *Journal of Geophysical Research: Planets*, 119, 2398–2415. <https://doi.org/10.1002/2014JE004620>
- Lynn, D. C., & Bonatti, E. (1965). Mobility of manganese in diagenesis of deep-sea sediments. *Marine Geology*, 3(6), 457–474. [https://doi.org/10.1016/0025-3227\(65\)90046-0](https://doi.org/10.1016/0025-3227(65)90046-0)
- Mahaffy, P. R., Webster, C. R., Cabane, M., Conrad, P. G., Coll, P., Atreya, S. K., et al. (2012). The sample analysis at Mars investigation and instrument suite. *Space Science Reviews*, 170(1–4), 401–478. <https://doi.org/10.1007/s11214-012-9879-z>
- Malin, M. C., & Edgett, K. S. (2000). Sedimentary rocks of early Mars. *Science*, 290(5498), 1927–1937. <https://doi.org/10.1126/science.290.5498.1927>
- Malin, M. C., Ravine, M. A., Caplinger, M. A., Ghaemi, F. T., Schaffner, J. A., Maki, J. N., et al. (2017). The Mars Science Laboratory (MSL) Mast cameras and Descent imager: Investigation and instrument descriptions. *Earth and Space Science*, 4, 506–539. <https://doi.org/10.1002/2016EA000252>
- Mangold, N., Dehouck, E., Fedo, C., Forni, O., Achilles, C., Bristow, T., et al. (2019). Chemical alteration of fine-grained sedimentary rocks at Gale Crater. *Icarus*, 321, 619–631. <https://doi.org/10.1016/j.icarus.2018.11.004>
- Maurice, S., Clegg, S. M., Wiens, R. C., Gasnault, O., Rapin, W., Forni, O., et al. (2016). ChemCam activities and discoveries during the nominal mission of the Mars Science Laboratory in Gale Crater, Mars. *Journal of Analytical Atomic Spectrometry*, 31(4), 863–889. <https://doi.org/10.1039/c5ja00417a>
- Maurice, S., Wiens, R. C., Saccoccio, M., Barraclough, B., Gasnault, O., Forni, O., et al. (2012). The ChemCam instrument suite on the Mars Science Laboratory (MSL) rover: Science objectives and mast unit description. *Space Science Reviews*, 170(1–4), 95–166. <https://doi.org/10.1007/s11214-012-9912-2>
- McAdam, A. C., Sutter, B., Archer, P. D., Franz, H. B., Wong, G. M., Lewis, J. M. T., et al. (2020). Constraints on the Mineralogy and Geochemistry of the Vera Rubin ridge, Gale crater, Mars, from Mars Science Laboratory Sample Analysis at Mars Evolved Gas Analyses. *Journal of Geophysical Research: Planets*, e2019JE006309. <https://doi.org/10.1029/2019JE006309>
- McLennan, S. M., Anderson, R. B., Bell, J. F., Bridges, J. C., Calef, F., Campbell, J. L., et al. (2014). Elemental geochemistry of sedimentary rocks at Yellowknife Bay, Gale Crater, Mars. *Science*, 343(6169), 1244734. <https://doi.org/10.1126/science.1244734>
- McLennan, S. M. (2000). Chemical composition of Martian soil and rocks: Complex mixing and sedimentary transport. *Geophysical Research Letters*, 27(9), 1335–1338. <https://doi.org/10.1029/1999GL008432>
- Meslin, P. Y., Gasda, P., L'Haridon, J., Forni, O., Lanza, N., Lamm, S., et al. (2018). *Detection of hydrous manganese and iron oxides with variable phosphorus and magnesium contents in the lacustrine sediments of the Murray Formation, Gale, Mars* (p. 1447). Paper presented at 49th Lunar and Planetary Science Conference.
- Milliken, R. E., Grotzinger, J. P., & Thomson, B. J. (2010). Paleoclimate of Mars as captured by the stratigraphic record in Gale Crater. *Geophysical Research Letters*, 37, L04201. <https://doi.org/10.1029/2009GL041870>

- Mischke, S., & Zhang, C. (2010). Holocene cold events on the Tibetan Plateau. *Global and Planetary Change*, 72(3), 155–163. <https://doi.org/10.1016/j.gloplacha.2010.02.001>
- Morris, R. V., Vaniman, D. T., Blake, D. F., Gellert, R., Chipera, S. J., Rampe, E. B., et al. (2016). Silicic volcanism on Mars evidenced by tridymite in high-SiO<sub>2</sub> sedimentary rock at Gale Crater. *Proceedings of the National Academy of Sciences*, 113(26), 7071–7076. <https://doi.org/10.1073/pnas.1607098113>
- Mouélic, S. L., Gasnault, O., Herkenhoff, K. E., Bridges, N. T., Langevin, Y., Mangold, N., et al. (2015). The ChemCam remote micro-imager at Gale Crater: Review of the first year of operations on Mars. *Icarus*, 249, 93–107. <https://doi.org/10.1016/j.icarus.2014.05.030>
- Nachon, M., Clegg, S. M., Mangold, N., Schröder, S., Kah, L. C., Dromart, G., et al. (2014). Calcium sulfate veins characterized by ChemCam/Curiosity at Gale Crater, Mars. *Journal of Geophysical Research: Planets*, 119, 1991–2016. <https://doi.org/10.1002/2013JE004588>
- Nachon, M., Mangold, N., Forni, O., Kah, L. C., Cousin, A., Wiens, R. C., et al. (2017). Chemistry of diagenetic features analyzed by ChemCam at Pahrump Hills, Gale Crater, Mars. *Icarus*, 281(121), 121–136. <https://doi.org/10.1016/j.icarus.2016.08.026>
- Nesbitt, H. W., & Young, G. M. (1982). Early Proterozoic climates and plate motions inferred from major element chemistry of lutites. *Nature*, 299(5885), 715–717. <https://doi.org/10.1038/299715a0>
- Ollila, A. M., Newsom, H. E., Clark, B., Wiens, R. C., Cousin, A., Blank, J. G., et al. (2014). Trace element geochemistry (Li, Ba, Sr, and Rb) using Curiosity's ChemCam: Early results for Gale Crater from Bradbury landing site to Rocknest. *Journal of Geophysical Research: Planets*, 119, 255–285. <https://doi.org/10.1002/2013JE004517>
- Palucis, M. C., Dietrich, W. E., Hayes, A. G., Williams, R. M. E., Gupta, S., Mangold, N., et al. (2014). The origin and evolution of the Peace Vallis fan system that drains to the Curiosity landing area, Gale Crater, Mars. *Journal of Geophysical Research: Planets*, 119, 705–728. <https://doi.org/10.1002/2013JE004583>
- Payré, V., Fabre, C., Cousin, A., Sautter, V., Wiens, R. C., Forni, O., et al. (2017). Alkali trace elements in Gale Crater, Mars, with ChemCam: Calibration update and geological implications. *Journal of Geophysical Research: Planets*, 122, 650–679. <https://doi.org/10.1002/2016JE005201>
- Rampe, E. B., Ming, D. W., Blake, D. F., Bristow, T. F., Chipera, S. J., Grotzinger, J. P., et al. (2017). Mineralogy of an ancient lacustrine mudstone succession from the Murray Formation, Gale Crater, Mars. *Earth and Planetary Science Letters*, 471, 172–185. <https://doi.org/10.1016/j.epsl.2017.04.021>
- Rampe, E. B., Bristow, T. F., Morris, R. V., Morrison, S. M., Achilles, C. N., Ming, D. W., et al. (2020). Mineralogy of Vera Rubin ridge from the Mars Science Laboratory CheMin Instrument. *Journal of Geophysical Research: Planets*, <https://doi.org/10.1029/2019je006306>
- Rapin, W., Ehlmann, B. L., Dromart, G., Schieber, J., Thomas, N. H., Fischer, W. W., et al. (2019). An interval of high salinity in ancient Gale Crater lake on Mars. *Nature Geoscience*, 12(11), 889–895. <https://doi.org/10.1038/s41561-019-0458-8>
- Rivera-Hernández, F., Sumner, D. Y., Mangold, N., Banham, S. G., Edgett, K. S., Fedo, C. M., et al. (2020). Grain size variations in the Murray Formation: Stratigraphic evidence for changing depositional environments in Gale Crater, Mars. *Journal of Geophysical Research: Planets*, 125, e2019JE006230. <https://doi.org/10.1029/2019JE006230>
- Rivera-Hernández, F., Sumner, D. Y., Mangold, N., Stack, K. M., Forni, O., Newsom, H., et al. (2019). Using ChemCam LIBS data to constrain grain size in rocks on Mars: Proof of concept and application to rocks at Yellowknife Bay and Pahrump Hills, Gale Crater. *Icarus*, 321, 82–98. <https://doi.org/10.1016/j.icarus.2018.10.023>
- Shao, J., & Yang, S. (2012). Does Chemical Index of Alteration (CIA) reflect silicate weathering and monsoonal climate in the Changjiang River Basin? *Chinese Science Bulletin*, 57(10), 1178–1187. <https://doi.org/10.1007/s11434-011-4954-5>
- Siebach, K. L., Fedo, C. M., Edgar, L. E., Edgett, K., Grotzinger, J. P., Fraeman, A. A., Thompson, L. M., et al. (2019). *Overview of Gale crater stratigraphy and sedimentology from 6 years of roving with Mars Science Laboratory* (p. 1479). Paper presented at 50th Lunar and Planetary Science Conference.
- Stack, K. M., Grotzinger, J. P., Lamb, M. P., Gupta, S., Rubin, D. M., Kah, L. C., et al. (2019). Evidence for plunging river plume deposits in the Pahrump Hills member of the Murray Formation, Gale Crater, Mars. *Sedimentology*, 66(5), 1768–1802. <https://doi.org/10.1111/sed.12558>
- Starkey, H. C. (1982). The role of clays in fixing lithium (No. 1278). U.S. Government Printing Office.
- Stein, N. T., Quinn, D. P., Grotzinger, J. P., Fedo, C., Ehlmann, B. L., Stack, K. M., et al. (2020). Regional structural orientation of the Mount Sharp group revealed by in situ dip measurements and stratigraphic correlations on the Vera Rubin ridge. *Journal of Geophysical Research: Planets*, 125, e2019JE006298. <https://doi.org/10.1029/2019JE006298>
- Sun, V. Z., Stack, K. M., Kah, L. C., Thompson, L., Fischer, W., Williams, A. J., et al. (2018). Late-stage diagenetic concretions in the Murray Formation, Gale Crater, Mars. *Icarus*, 321, 866–890. <https://doi.org/10.1016/j.icarus.2018.12.030>
- Thompson, L. M., Fraeman, A. A., Berger, J. A., Rampe, E. B., Boyd, N. I., Gellert, R., et al. (2019). Compositional characteristics and trends within the Vera Rubin ridge, Gale Crater, Mars as determined by APXS: Sedimentary, diagenetic and alteration history (p. 3269). Paper presented at the 50th Lunar and Planetary Science Conference, The Woodlands, TX.
- Thomson, B. J., Bridges, N. T., Milliken, R., Baldrige, A., Hook, S. J., Crowley, J. K., et al. (2011). Constraints on the origin and evolution of the layered mound in Gale Crater, Mars using Mars reconnaissance orbiter data. *Icarus*, 214(2), 413–432. <https://doi.org/10.1016/j.icarus.2011.05.002>
- Thorpe, M. T., Bristow, T. F., Rampe, E. B., Grotzinger, J. P., Fox, V. K., Bennett, K. A., et al. (2020). *Glen Torridon mineralogy and the sedimentary history of the clay mineral bearing unit* (p. 1524). Paper presented at 51st Lunar and Planetary Science Conference.
- Turner, S. M. R., Schwenzler, S. P., Bridges, J. C., Bedford, C. C., Rampe, E. B., Fraeman, A. A., et al. (2019). *Thermochemical modelling of fluid-rock reactions in Vera Rubin ridge, Gale crater, Mars* (p. 1897). Paper presented at 50th Lunar and Planetary Science Conference, The Woodlands, TX.
- Villumsen, A., & Nielsen, O. B. (1976). The influence of palaeosalinity, grain size distribution and clay minerals on the content of B, Li and Rb in Quaternary sediments from eastern Jutland, Denmark. *Sedimentology*, 23(6), 845–855. <https://doi.org/10.1111/j.1365-3091.1976.tb00112.x>
- Vine, J. D. (1980). Where on Earth is all the lithium? (Open-File Report 80–1234).
- Wiens, R. C., Maurice, S., Lasue, J., Forni, O., Anderson, R. B., Clegg, S., et al. (2013). Pre-flight calibration and initial data processing for the ChemCam laser-induced breakdown spectroscopy instrument on the Mars Science Laboratory rover. *Spectrochimica Acta Part B: Atomic Spectroscopy*, 82, 1–27. <https://doi.org/10.1016/j.sab.2013.02.003>
- Wiens, R. C., Maurice, S., Barraclough, B., Saccoccio, M., Barkley, W. C., Bell, J. F., et al. (2012). The ChemCam instrument suite on the Mars Science Laboratory (MSL) Rover: Body unit and combined system tests. *Space Science Reviews*, 170(1–4), 167–227. <https://doi.org/10.1007/s11214-012-9902-4>

- Wong, G. M., Lewis, J. M. T., Knudson, C. A., Millan, M. S. A., McAdam, A. C., Eigenbrode, J. L., et al. (2020). Detection of reduced sulfur on Vera Rubin ridge by quadratic discriminant analysis of volatiles observed during evolved gas analysis. *Journal of Geophysical Research: Planets*, e2019JE006304. <https://doi.org/10.1029/2019JE006304>
- Yen, A. S., Ming, D. W., Vaniman, D. T., Gellert, R., Blake, D. F., Morris, R. V., et al. (2017). Multiple stages of aqueous alteration along fractures in mudstone and sandstone strata in Gale Crater, Mars. *Earth and Planetary Science Letters*, 471, 186–198. <https://doi.org/10.1016/j.epsl.2017.04.033>